The Vertical City Weather Generator (VCWG v1.1.0)

Mohsen Moradi[1], Benjamin Dyer[2], Amir Nazem[1], Manoj K. Nambiar[1], M. Rafsan Nahian[1], Bruno Bueno[5], Chris Mackey[7], Saeran Vasanthakumar[8], Negin Nazarian[3], E. Scott Krayenhoff[4], Leslie K. Norford[6], and Amir A. Aliabadi[1]

[1]School of Engineering, University of Guelph, Guelph, Canada
[2]Department of Physics and Astronomy, McMaster University, Hamilton, Canada
[3]Built Environment, University of New South Wales, Sydney, Australia
[4]School of Environmental Sciences, University of Guelph, Guelph, Canada
[5]Fraunhofer Institute for Solar Energy Systems ISE, Freiburg, Germany
[6]Department of Architecture, Massachusetts Institute of Technology, Cambridge, USA
[7]Ladybug Tools LLC, Boston, USA
[8]Kieran Timberlake Research Group, Philadelphia, USA

Correspondence: Amir A. Aliabadi (aliabadi@uoguelph.ca)

Abstract. The Vertical City Weather Generator (VCWG) is a computationally efficient urban microclimate model developed to predict temporal and vertical variation of temperature, wind speed, and specific humidity. It is composed of various sub models: a rural model, an urban microclimate model, and a building energy model. In a nearby rural site, the Monin-Obukhov Similarity Theory (MOST) is used to solve for the vertical profile of potential temperature and friction velocity at 10 m elevation, which is forced with weather data. The rural model also calculates a horizontal pressure gradient. The rural model outputs are then forced on a vertical diffusion urban microclimate model that solves vertical transport equations for momentum, temperature, and specific humidity. The urban microclimate model is also coupled to a building energy model using two-way interaction. The aerodynamic and thermal effects of urban elements and vegetation are considered in VCWG. To evaluate the VCWG model, a microclimate field campaign was held in Guelph, Canada, from 15 July 2018 to 5 September 2018. The meteorological measurements were carried out under a comprehensive set of wind directions, wind speeds, and thermal stability conditions in both the rural and the nearby urban areas. The model evaluation indicates that the VCWG predicts vertical profiles of meteorological variables in reasonable agreement with field measurements. The average BIAS for wind speed, temperature and specific humidity is 1.06 $\mathrm{ms^{-1}}$, -1.43 K, and 0.005 $\mathrm{kgkg^{-1}}$, respectively. The modeled and observed Urban Heat Island (UHI) values are in agreement. VCWG-predicted mean and standard deviation for UHI are +1.20 and 1.53K, respectively, in reasonable agreement with observations reporting a mean and deviation for UHI of +1.08 and 1.23 K, respectively. The performance of the model is further explored to investigate the effects of urban configurations such as plan and frontal area densities, varying levels of vegetation, building energy configuration, radiation configuration, seasonal variations, different climate zones, and time series analysis on the model predictions. The results obtained from the explorations are reasonably consistent with previous studies in the literature, justifying the reliability and computational efficiency of VCWG for operational urban development projects.

1 Introduction

Urban areas interact with the atmosphere through various exchange processes of heat, momentum, and mass, which substantially impact the human comfort, air quality, and urban energy consumption. Such complex interactions are observable from the Urban Canopy Layer (UCL) to a few hundred meters within the Atmospheric Boundary Layer (ABL) (Britter and Hanna, 2003). Modeling enables a deeper understanding of interactions between urban areas and the atmosphere and can possibly offer solutions toward mitigating adverse effects of urban development on the climate. A brief review of modeling efforts is essential toward more accurate model development for the understanding of urban areas-atmosphere interactions.

Mesoscale models incorporating the urban climate were initially aimed to resolve weather features with grid resolutions of at best few hundred meters horizontally and a few meters vertically, without the functionality to resolve microscale three-dimensional flows or to account for atmospheric interactions with specific urban elements such as roads, roofs, and walls (Bornstein, 1975). These models usually consider the effect of built-up areas by introducing an urban aerodynamic roughness length (Grimmond and Oke, 1999) or adding source or sink terms in the momentum (drag) and energy (anthropogenic heat) equations (Dupont et al., 2004). Therefore, if higher grid resolutions less than ten meters (horizontal and vertical) are desired (Moeng et al., 2007; Wang et al., 2009; Talbot et al., 2012), microscale climate models should be deployed. Some efforts also have begun to develop multiscale climate models by coupling mesoscale and microscale models (Chen et al., 2011; Conry et al., 2014; Kochanski et al., 2015; Mauree et al., 2018). Numerous studies have used Computational Fluid Dynamics (CFD) to investigate the urban microclimate taking into account interactions between the atmosphere and the urban elements with full three-dimensional flow analysis (Saneinejad et al., 2012; Blocken, 2015; Nazarian and Kleissl, 2016; Aliabadi et al., 2017; Nazarian et al., 2018). Despite accurate predictions, CFD models are not computationally efficient, particularly for weather forecasting at larger scales and for a long period of time, and they usually do not represent many processes in the real atmosphere such as clouds and precipitation. As an alternative, UCMs require understanding of the interactions between the atmosphere and urban elements to parameterize various exchange processes of radiation, momentum, heat, and moisture within and just above the canopy, based on experimental data (Masson, 2000; Kusaka et al., 2001; Chin et al., 2005; Aliabadi et al., 2019), three-dimensional simulations, or simplified urban configurations (Martilli et al., 2002; Coceal and Belcher, 2004; Krayenhoff et al., 2014, 2015; Nazarian and Kleissl, 2016). These urban canopy models are more computationally efficient than CFD models. They are designed to provide more details on heat storage and radiation exchange, while they employ less detailed flow calculations.

Urban microclimate models must account for a few unique features of the urban environment. Urban obstacles such as trees and buildings contribute substantially to the changing of flow and turbulence patterns in cities (Kastner-Klein et al., 2004). Difficulties arise when the spatially inhomogeneous urban areas create highly three-dimensional wind patterns that result in the difficulty of parameterizations (Roth, 2000; Resler et al., 2017). For example, the surfaces of urban obstacles exert form and skin drag and consequently alter flow direction and produce eddies at different spatiotemporal scales. This can lead to the formation of shear layers at roof level with variable oscillation frequencies (Tseng et al., 2006; Masson et al., 2008; Zajic et al., 2011), all of such phenomena should be properly approximated in parameterizations.

Heat exchanges between the indoor and outdoor environments significantly influence the urban microclimate. Various studies have attempted to parametrize heat sources and sinks caused by buildings such as heat fluxes due to infiltration, exfiltration, ventilation, walls, roofs, roads, windows, and building energy systems (Kikegawa et al., 2003; Salamanca et al., 2010; Yaghoobian and Kleissl, 2012). Therefore, a Building Energy Model (BEM) is required to be properly integrated in an urban microclimate model to take account of the impact of building energy performance on the urban microclimate (Bueno et al., 2011, 2012b; Gros et al., 2014). This two-way interaction between the urban microclimate and indoor environment can significantly affect Urban Heat Island (UHI) and energy consumption of buildings (Adnot et al., 2003; Salamanca et al., 2014).

Urban vegetation can substantially reduce the adverse effects of UHI, particularly during heat waves, resulting in more thermal comfort (Grimmond et al., 1996; Akbari et al., 2001; Armson et al., 2012). Urban trees can potentially provide shade and shelter, and, therefore, change the energy balance of the individual buildings as well as the entire city (Akbari et al., 2001). A study of the local-scale surface energy balance revealed that the amount of energy dissipated due to the cooling effect of trees is not negligible and should be parameterized properly (Grimmond et al., 1996). In addition, the interaction between urban elements, most importantly trees and buildings, is evident in radiation trapping within the canyon and most importantly shading impact of trees (Krayenhoff et al., 2014; Redon et al., 2017; Broadbent et al., 2019). Buildings and trees obstruct the sky with implications in long and shortwave radiation fluxes downward and upward that may create unpredictable diurnal and seasonal changes in UHI (Futcher, 2008; Kleerekoper et al., 2012; Yang and Li, 2015). Also, it has been shown that not only trees but also the fractional vegetation coverage on urban surfaces can alter urban temperatures with implications in UHI (Armson et al., 2012). Trees, particularly those which are shorter than buildings, also exert drag and alter flow patterns within the canopy, however, this effect is not as significant as that drag induced by buildings (Krayenhoff et al., 2015). Such complex interactions must be accounted for in successful urban microclimate models.

1.1 Research Gaps

Numerous studies have focused on high fidelity urban microclimate models with high spatiotemporal flow resolution, capturing important features of the urban microclimate with acceptable accuracy (Gowardhan et al., 2011; Soulhac et al., 2011; Blocken, 2015; Nazarian et al., 2018). Some example Computational Fluid Dynamics (CFD) models of this kind include Open-source Field Operation And Manipulation (OpenFOAM) (Aliabadi et al., 2017, 2018), Parallelized Large-Eddy Simulation Model (PALM) (Maronga et al., 2015; Resler et al., 2017), and ENVI-met (Crank et al., 2018). Despite the advances, however, high fidelity models capable of resolving three-dimensional flows at microscale are not computationally efficient and they are complex to implement for operational applications. As a remedy, lower-dimensional flow urban microclimate models have been developed with many practical applications in city planning, architecture, and engineering consulting. For example, bulk flow (single-layer) models such as Urban Weather Generator (UWG) calculate the flow dynamics in one point, usually the centre of a hypothetical urban canyon, which is representative of all locations (Mills, 1997; Kusaka et al., 2001; Salamanca et al., 2010; Ryu et al., 2011; Bueno et al., 2012a, 2014). Another bulk flow (single-layer) model is Canyon Air Temperature (CAT) model, which utilizes standard data from a meteorological station to estimate air temperature in a street canyon (Erell and Williamson, 2006). The Town Energy Balance (TEB) calculates energy balances for urban surfaces, which is forced by meteorological data and incoming solar radiation in the urban site with no connection to rural meteorological conditions (Masson et al., 2002). The Temperatures of Urban Facets - 3D (TUF-3D) model calculates urban surface temperatures with the main focus on three-dimensional radiation exchange, but it adopts bulk flow (single-layer) modeling without a connection to the surrounding rural area (Krayenhoff and Voogt, 2007). More recently TUF-3D was coupled to an Indoor-Outdoor Building Energy Simulator (TUF-3D-IOBES), but still this model adopted a bulk flow (single-layer) parameterization (Yaghoobian and Kleissl, 2012). The multi-layer Building Effect Parametrization-Tree (BEP-Tree) model includes variable building heights, the vertical variation of climate variables and the effects of trees, but it is not linked to a building energy model (Martilli et al., 2002; Krayenhoff, 2014; Krayenhoff et al., 2020). More recently, the BEP model has been coupled to a Building Energy Model (BEP+BEM) but it is forced with meteorological variables from higher altitudes above a city using mesoscale models, instead of near surface meteorological variables measured outside the city (rural areas). An overview of the literature reveals an apparent paucity of an independent urban microclimate model that accounts for some spatiotemporal variation of meteorological parameters in the urban environment and considers the effects of trees, building energy, radiation, and the connection to the near-surface rural meteorological conditions measured outside a city, without the need for mesoscale modeling, computationally efficiently and is operationally simple for practical applications.

1.2 Objectives

In this study, we present a new urban microclimate model, called the Vertical City Weather Generator (VCWG), which attempts to overcome some of the limitations mentioned in the previous section. It resolves vertical profiles (the direction in which turbulent transport is significant) of climate parameters, such as temperature, wind, and humidity, in relation to urban design parameters. VCWG also includes a building energy model. It allows parametric investigation of design options on urban climate control at multiple heights, particularly if high density and high-rise urban design options are considered. This is a significant advantage over the bulk flow (single-layer) models such as UWG, which only consider one point for flow dynamics inside a hypothetical canyon (Masson, 2000; Kusaka et al., 2001; Dupont et al., 2004; Krayenhoff and Voogt, 2007; Lee and Park, 2008; Bueno et al., 2012a, 2014). The VCWG is designed to cycle through different atmospheric stability conditions that could be observed over the course of a day, but it is very computationally efficient with the capability to be run up to and beyond an entire year. The advantages of VCWG are as follows. 1) It does not need to be coupled to a mesoscale weather model because it functions standalone as a microclimate model. 2) Unlike many UCMs that are forced with climate variables above the urban roughness sublayer (e.g. TUF-3D), VCWG is forced with rural climate variables measured at 2m (temperature and humidity) and 10m (wind) elevation that are widely accessible and available around the world, making VCWG highly practical for urban design investigations in different climates. 3) VCWG provides urban climate information in one dimension, i.e. resolved vertically. This is advantageous over bulk flow (single-layer) models because vertical transport of momentum, heat, and atmospheric species is significantly important. 4) VCWG is coupled with the building energy model using two-way interaction.

To evaluate the model, a microclimate field campaign in a representative urban area and a surrounding rural area was held in Guelph, Canada, during the Summer of 2018. Three components of wind velocity, temperature, relative humidity, and solar radiation were rigorously measured in this field campaign at different locations and under a comprehensive set of wind speeds, wind directions, and atmospheric stability conditions. To explore the model, the VCWG is set to run to investigate the effects of building dimensions, urban vegetation, building energy configuration, radiation configuration, seasonal variations, other climates, and time series analysis on the model outcome.

1.3 Organization of the Article

The paper is structured as follows. Section 2 describes the methodology. In Sect. 2.1, all components of the VCWG and the way that they are integrated are presented. First, the Energy Plus Weather (EPW) dataset is introduced, which is the background rural weather data used to force VCWG. Next, the Rural Model (RM), used to determine the potential temperature profile, friction velocity, and the horizontal pressure gradient in the rural area, is described. Then, details are discussed for the one-dimensional vertical diffusion model for the urban environment, the building energy model, and the radiation model, which are forced by the RM to predict the vertical profiles of meteorological quantities in the urban area. Section 2.2 describes the location and details of the field campaign, including meteorological instruments used. Section 3 provides the results and discussion. It starts with the evaluation of VCWG by comparing simulation results with those of the field measurements in Sect. 3.1. Then, results from other explorations including effects of building dimensions, foliage density, building energy configuration, radiation configuration, seasonal variation, different climate zones, and time series analysis on urban climate are presented in Sect. 3.2. Finally, Sect. 4 is devoted to conclusions and future work. Additional information about the equations used in the model and the details about the VCWG software are provided in the appendix.

2 Methodology

2.1 Vertical City Weather Generator (VCWG)

Figure 1 shows the VCWG model schematic. VCWG consists of four integrated sub models. 1) a Rural Model (RM) (Sect. 2.1.2) forces meteorological boundary conditions on VCWG based on Monin-Obukhov similarity theory (Businger et al., 1971; Dyer, 1974) and a soil heat transfer model (Bueno et al., 2012a, 2014). 2) a one-dimensional vertical diffusion model (Sect. 2.1.3) is used for calculation of the urban potential temperature, wind speed, turbulence kinetic energy, and specific humidity profiles, considering the effect of trees. This model was initially developed by Santiago and Martilli (2010) and Simón-Moral et al. (2017), while it was later ingested into another model called the Building Effect Parametrization with Trees (BEP-Tree), considering the effects of trees (Krayenhoff, 2014; Krayenhoff et al., 2015, 2020). 3) a Building Energy Model (BEM) (Sect. 2.1.4) is used to determine the sensible and latent waste heats of buildings imposed on the urban environment. This model is a component of the Urban Weather Generator (UWG) model (Bueno et al., 2012a, 2014). 4) a radiation model with vegetation (Sect. 2.1.5) is used to compute the longwave (Loughner et al., 2012) and shortwave (Redon et al., 2017) heat exchanges between the urban canyon and the atmosphere/sky.

The sub models are integrated to predict vertical variation of urban microclimate parameters including potential temperature, wind speed, specific humidity, and turbulence kinetic energy as influenced by aerodynamic and thermal effects of urban elements including longwave and shortwave radiation exchanges, sensible heat fluxes released from urban elements, cooling effect of trees, and the induced drag by urban obstacles. The Rural Model (RM) takes latitude, longitude, dry bulb temperature, relative humidity, dew point temperature, and pressure at $2\ \mathrm{m}$ elevation, wind speed and direction at $10\ \mathrm{m}$ elevation, down-welling direct radiation, and down-welling diffuse radiation from an Energy Plus Weather (EPW) file. For every time step, and forced with the set of weather data, the RM then computes a potential temperature profile, a constant specific humidity profile, and a horizontal pressure gradient, all of which are forced as boundary conditions to the one-dimensional vertical diffusion model in the urban area. The potential temperature and specific humidity are forced as fixed values on top of the domain for the urban vertical diffusion model in the temperature and specific humidity equations, respectively. The horizontal pressure gradient is forced as a source term for the urban vertical diffusion model in the momentum equation. While forced by the RM, the urban one-dimensional vertical diffusion model is also coupled with a building energy model and the two-dimensional radiation model. The three models have feedback interaction and converge to a potential temperature solution iteratively. The urban one-dimensional vertical diffusion model calculates the flow quantities at the centre of control volumes, which are generated by splitting the urban computational domain into multiple layers within an above the urban canyon (see Fig. 2). The urban domain extends to five times building height that conservatively includes the entire atmospheric roughness sublayer (Santiago and Martilli, 2010; Aliabadi et al., 2017). The feedback interaction coupling scheme among the building energy model, radiation model, and the urban one-dimensional vertical diffusion model is designed to update the boundary conditions, surfaces temperatures, and the source/sink terms in the transport equations. For each time step, the iterative calculations for all the sub models continue until the convergence criterion of potential temperature in the canyon are fulfilled. More details about the sub models are provided in the subsequent sections and the appendix.

2.1.1 Energy Plus Weather Data

Building energy and solar radiation simulations are typically carried out with standardized weather files. Energy Plus Weather (EPW) files include recent weather data for 2100 locations and are saved in the standard EnrgyPlus format, developed by US department of energy.[1] The data is available for most North American cities, European cities, and other regions around the World. The weather data are arranged by World Meteorological Organization (WMO) based on region and country. An EPW file contains typical hourly-based data of meteorological variables. The meteorological variables are dry bulb temperature, dew point temperature, relative humidity, incoming direct and diffusive solar radiation fluxes from sky, wind direction, wind speed, sky condition, precipitation, and general information about field logistics and soil properties. Precipitation data is often missing in the EPW files, which affects calculation of latent heat in the rural area.

[1] https://energyplus.net/weather

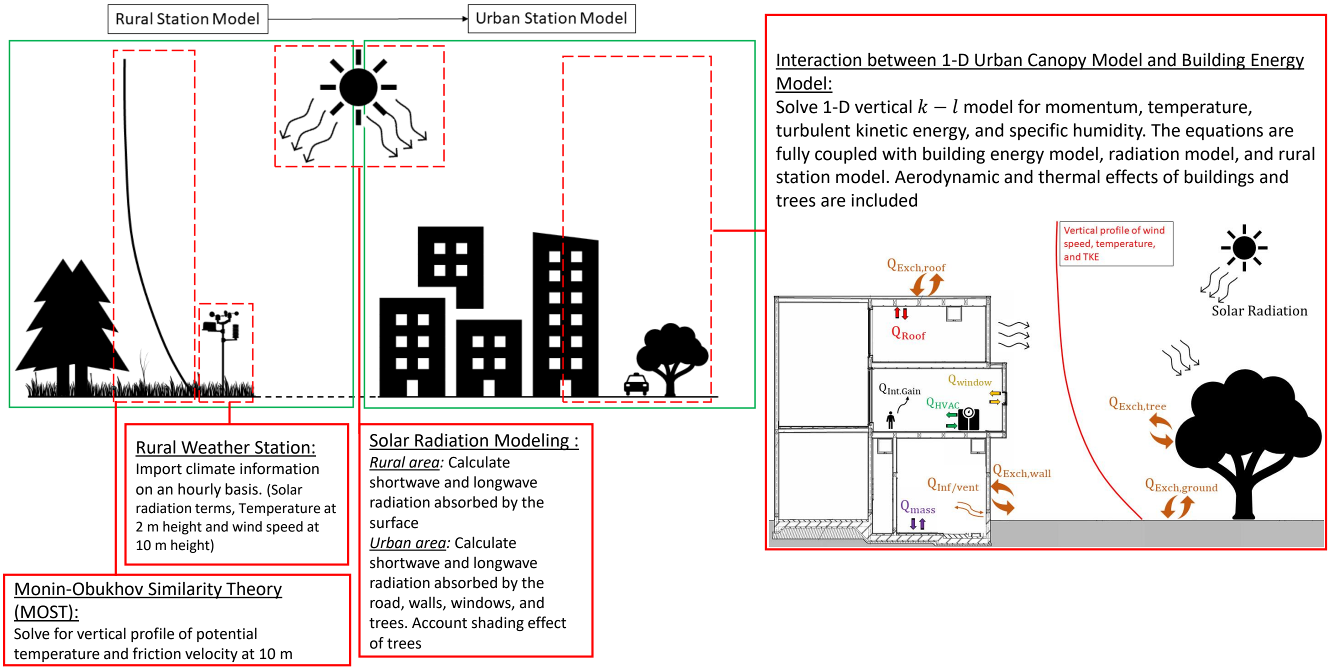

Figure 1. The schematic of Vertical City Weather Generator (VCWG).

2.1.2 Rural Model

In the rural model, the Monin–Obukhov Similarity Theory (MOST) is used to solve for the vertical profile of potential temperature and friction velocity at $10\ \mathrm{m}$ elevation using meteorological measurements near the surface. MOST is usually applied to the atmospheric surface layer over flat and homogeneous lands to describe the vertical profiles of wind speed, potential temperature, and specific humidity as functions of momentum flux, sensible heat flux, and latent heat flux measured near the surface, respectively. Using MOST the gradient of potential temperature is given by

$$\frac{\partial \overline{\Theta}_{rur}}{\partial z} = \frac{Q_{net,rur}}{\rho C_p \kappa u_* z} \Phi_H \left(\frac{z}{L}\right), \tag{1}$$

where $\overline{\Theta}_{\mathrm{rur}}$ is mean potential temperature in the rural area, $\mathrm{Q}_{\mathrm{net,rur}}$ is net rural sensible heat flux, ρ is air density near the rural surface, C_{p} is air specific heat capacity, u_* is friction velocity, and κ is the von Kármán constant. Φ_{H} is known as the universal dimensionless temperature gradient. This terms was estimated for different thermal stability conditions based on experimental data by (Businger et al., 1971; Dyer, 1974)

$$\Phi_H\left(\frac{z}{L}\right) = \begin{cases} 0.74 + 4.7\frac{z}{L}, & \frac{z}{L} > 0(\text{Stable}) \\ 0.74, & \frac{z}{L} = 0(\text{Neutral}) \\ 0.74\left(1 - \frac{9z}{L}\right)^{-1/4}, & \frac{z}{L} < 0(\text{Unstable}). \end{cases} \tag{2}$$

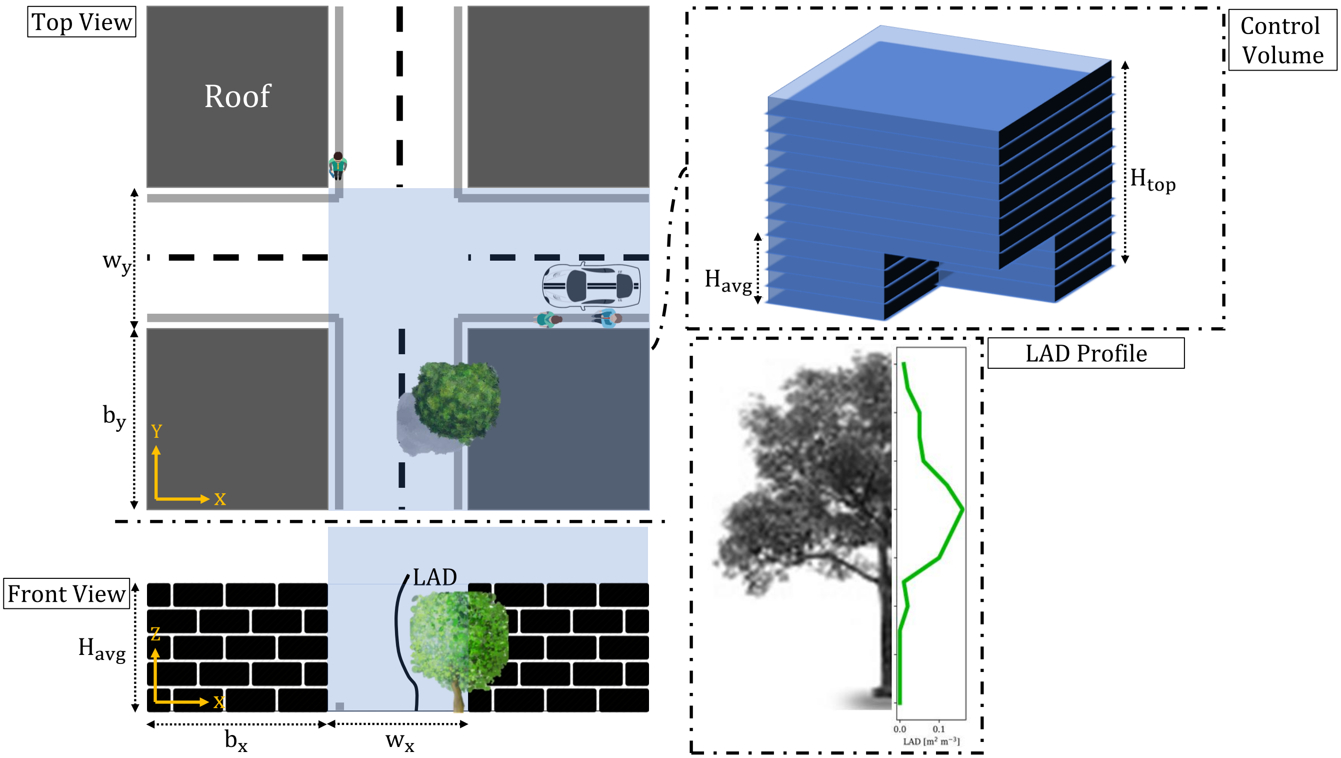

Figure 2. Simplified urban area used in VCWG and corresponding layers of control volumes within and above the canyon. The height of the domain is five times of the average building height.

In the dimensionless stability parameter z/L, z is height above ground and L is Obukhov-Length given by

$$L = \frac{-\overline{\Theta}_{rur,z=2m} u_*^3}{g\kappa \frac{Q_{net,rur}}{\rho C_p}}. \tag{3}$$

It has been observed that there is a monotonic reduction in friction velocity with increasing stratification (Joffre et al., 2001). So, friction velocity in Eq. 1 is estimated from momentum flux generalization (Monin and Obukhov, 1957)

$$\frac{\partial \overline{S}_{rur}}{\partial z} = \frac{u_*}{\kappa z} \Phi_M \left(\frac{z}{L}\right), \tag{4}$$

where $\overline{S}_{rur}$ is the mean horizontal wind speed in the rural area and Φ_M is the universal dimensionless wind shear and is estimated for different thermal stability conditions based on experimental data (Businger et al., 1971; Dyer, 1974)

$$\Phi_M\left(\frac{z}{L}\right) = \begin{cases} 1 + 4.7\frac{z}{L}, & \frac{z}{L} > 0 (\text{Stable}) \\ 1, & \frac{z}{L} = 0 (\text{Neutral}) \\ \left(1 - \frac{15z}{L}\right)^{-1/4}, & \frac{z}{L} < 0 (\text{Unstable}). \end{cases} \tag{5}$$

Friction velocity can be determined by numerically integrating Eq. 4 from the elevation of the rural aerodynamic roughness length $\mathrm{z_0}$ to $10\ \mathrm{m}$ in an iterative process. This method provides a friction velocity that is corrected for thermal stability effects. The potential temperature profiles are also obtained by numerical integration of Eq. 1.

Meteorological information obtained from the weather station including direct and diffuse solar radiation, temperature at the $2\ \mathrm{m}$ elevation, and wind speed at $10\ \mathrm{m}$ elevation are used to calculate the net sensible heat flux at the surface

$$Q_{net,rur} = \underbrace{Q_{Hveg,rur} + h_{conv}(T_{0,rur} - T_{air,rur}) + Q_{rad,rur}}_{\text{sensible heat flux}}, \tag{6}$$

where $\mathrm{Q_{net,rur}}$ is the net sensible heat flux (positive upward from the surface into the atmosphere at the rural site), $\mathrm{Q_{Hveg,rur}}$ is the sensible heat flux from biogenic activity of vegetation (Ciccioli et al., 1997; van der Kooi et al., 2019), $\mathrm{h_{conv}}$ is the convection heat transfer coefficient at the surface, $\mathrm{T_{0,rur}}$ is the rural surface temperature calculated by the rural model, $\mathrm{T_{air,rur}}$ is the air temperature at $2\ \mathrm{m}$ elevation, and $\mathrm{Q_{rad,rur}}$ is the longwave and shortwave radiation absorbed by rural surface (for more details see Appendix A). Numerous studies have focused on parameterization of convection heat transfer coefficient reviewed by Palyvos (2008). In this study, the following boundary-layer type correlation between $\mathrm{h_{conv}}$ and mean wind speed ($\mathrm{\overline{S}_{rur,z=10m}}$) is used

$$h_{conv} = 3.7\overline{S}_{rur} + 5.8. \tag{7}$$

The rural model also outputs a horizontal pressure gradient based the friction velocity calculation that is later used as a source term for the urban one-dimensional vertical diffusion momentum equation. The pressure gradient is parameterized as $\rho \mathrm{u_*^2/H_{top}}$, where $\mathrm{H_{top}}$ is the height of the top of the domain, here five times the average building height (Krayenhoff et al., 2015; Nazarian et al., 2019).

Another assumption made in the rural model is that the specific humidity is constant in the vertical direction, i.e. invariant with height, for the lowest range of the atmospheric surface layer. This assumption is made, for lack of a better assumption, because with only surface data and lack of latent heat flux, it is not practical to calculate variation of specific humidity with height in the surface layer.

A density profile is required to convert the real temperature profile in the rural area ($\mathrm{T_{rur}}$) to potential temperature profile and vice versa, which is used in the Eq. 1. Using a reference density (ρ_0), reference temperature ($\mathrm{T_0}$), and reference pressure ($\mathrm{P_0}$) at the surface level from the weather station at 2 m elevation, and considering a lapse rate of $-0.000133\ \mathrm{kg\ m^{-3}\ m^{-1}}$ for density within the surface layer, the density profile can be simplistically parameterized by $\rho = \rho_0 - 0.000133(z - z_0)$.

After calculating potential temperature and specific humidity at the top of the domain by the rural model, these values can be applied as fixed-value boundary condition at the top of the domain in the urban one-dimensional vertical diffusion model in the energy and specific humidity transport equations.

2.1.3 Urban Vertical Diffusion Model

Numerous studies have attempted to parameterize the interaction between urban elements and the atmosphere in terms of dynamical and thermal effects, from very simple models based on MOST (Stull, 1988), to the bulk flow (single-layer) parameterizations (Krayenhoff and Voogt, 2007; Masson, 2000; Kusaka et al., 2001; Bueno et al., 2014), to multi-layer models (Hamdi and Masson, 2008; Santiago and Martilli, 2010; Krayenhoff et al., 2015, 2020) with different levels of complexity. The multi-layer models usually treat aerodynamic and thermal effects of urban elements as sink or source terms in momentum, heat, specific humidity, and turbulence kinetic energy equations. Parameterization of the exchange processes between the urban elements and the atmosphere can be accomplished using either experimental data or CFD simulations (Martilli et al., 2002; Dupont et al., 2004; Kondo et al., 2005; Kono et al., 2010; Lundquist et al., 2010; Santiago and Martilli, 2010; Krayenhoff et al., 2015; Aliabadi et al., 2019). CFD-based parameterizations proposed by Martilli and Santiago (2007), Santiago and Martilli (2010), Krayenhoff et al. (2015), Nazarian et al. (2019) use results from Reynolds-Averaged Navier-Stokes (RANS) or Large-Eddy Simulations (LES) including effects of trees and buildings. These parameterizations consider the CFD results at different elevations after being temporally and horizontally averaged.

For the one-dimensional vertical diffusion model, any variable such as cross- and along-canyon wind velocities (U and V, respectively), potential temperature (Θ), and specific humidity (Q) is presented using Reynolds averaging. The one-dimensional time-averaged momentum equations in the cross- and along-canyon components can be shown as (Santiago and Martilli, 2010; Krayenhoff, 2014; Krayenhoff et al., 2015; Simón-Moral et al., 2017; Nazarian et al., 2019; Krayenhoff et al., 2020)

$$\frac{\partial \overline{U}}{\partial t} = -\underbrace{\frac{\partial \overline{uw}}{\partial z}}_{I} - \underbrace{\frac{1}{\rho}\frac{\partial \overline{P}}{\partial x}}_{II} - \underbrace{D_x}_{III}, \tag{8}$$

$$\frac{\partial \overline{V}}{\partial t} = -\underbrace{\frac{\partial \overline{vw}}{\partial z}}_{I} - \underbrace{\frac{1}{\rho}\frac{\partial \overline{P}}{\partial y}}_{II} - \underbrace{D_y}_{III}, \tag{9}$$

where $\overline{\mathrm{P}}$ is time-averaged pressure. The terms on the right hand side of Eqs. 8 and 9 are the vertical gradient of turbulent flux of momentum (I), acceleration due to the large-scale pressure gradient (II), and the sum of pressure, building form, building skin, and vegetation drag terms (III). The parameterization of the latter term is detailed in Appendix A and is not reported here for brevity. K-theory was used to parameterize the vertical momentum fluxes, i.e. $\partial\overline{uw}/\partial z = -K_m \partial\overline{U}/\partial z$ and $\partial\overline{vw}/\partial z = -K_m \partial\overline{V}/\partial z$ (the same approach will be used in energy and humidity equations), where the diffusion coefficient is calculated using a $\mathrm{k}-\ell$ model

$$K_m = C_k \ell_k k^{1/2}, \tag{10}$$

where $\mathrm{C_k}$ is a constant and ℓ_k is a length scale optimized using sensitivity analysis based on CFD (Nazarian et al., 2019). $\mathrm{C_k}$ can be obtained based on the bulk Richardson number $\mathrm{Ri_b{=}gH_{avg}}\Delta\overline{\Theta}/(\Delta\overline{\mathrm{S}}^2\overline{\Theta}_\mathrm{avg})$, where g is gravitational acceleration, $\mathrm{H_{avg}}$ is average building height, $\Delta\overline{\Theta}$ and $\Delta\overline{\mathrm{S}}$ are the variation of temperature and horizontal wind speed over vertical distance $\mathrm{H_{avg}}$ (i.e. roof level minus street level), and $\overline{\Theta}_\mathrm{avg}$ is the mean temperature in the canyon. $\mathrm{C_k}$ was determined depending on a critical bulk Richardson number, which is set to 0.25. The value $\mathrm{C_k}$=2 is used for unstable condition ($\mathrm{Ri_b} > 0.25$) and $\mathrm{C_k}$=1 is used for stable condition ($\mathrm{Ri_b} < 0.25$). More details on $\mathrm{C_k}$ and ℓ_k are provided in Krayenhoff (2014) and Nazarian et al. (2019). The turbulence kinetic energy k can be calculated using a prognostic equation (Krayenhoff et al., 2015)

$$\frac{\partial k}{\partial t} = \underbrace{K_m\left[\left(\frac{\partial \overline{U}}{\partial z}\right)^2 + \left(\frac{\partial \overline{V}}{\partial z}\right)^2\right]}_{I} + \underbrace{\frac{\partial}{\partial z}\left(\frac{K_m}{\sigma_k}\frac{\partial k}{\partial z}\right)}_{II} - \underbrace{\frac{g}{\Theta_0}\frac{K_m}{Pr_t}\frac{\partial \overline{\Theta}}{\partial z}}_{III} + \underbrace{S_{wake}}_{IV} - \underbrace{\varepsilon}_{V}, \tag{11}$$

where g is acceleration due to gravity and Θ_0 is a reference potential temperature. The terms on the right hand side of Eq. 11 are shear production (I), turbulent transport of kinetic energy parameterized based on K-theory (II), buoyant production/dissipation (III), wake production by urban obstacles (IV), and dissipation (V). Parameterization of the last two terms is presented in more detail in Appendix A and Krayenhoff (2014) and not reported here for brevity. σ_k is turbulent Prandtl number for kinetic energy, which is generally suggested to be σ_k=1 (Pope, 2000).

To calculate vertical profile of potential temperature in the urban area, the transport equation can be derived as

$$\frac{\partial \overline{\Theta}}{\partial t} = \underbrace{\frac{\partial}{\partial z}\left(\frac{K_m}{Pr_t}\frac{\partial \overline{\Theta}}{\partial z}\right)}_{I} + \underbrace{S_{\Theta R} + S_{\Theta G} + S_{\Theta W} + S_{\Theta V} + S_{\Theta A} + S_{\Theta waste}}_{II}, \tag{12}$$

where the first term on the right hand side is turbulent transport of heat (I) and the heat sink/source terms (II) correspond to sensible heat exchanges with roof ($\mathrm{S_{\Theta R}}$), ground ($\mathrm{S_{\Theta G}}$), wall ($\mathrm{S_{\Theta W}}$), urban vegetation $\mathrm{S_{\Theta V}}$, and radiative divergence $\mathrm{S_{\Theta A}}$ detailed in appendix A and by Krayenhoff (2014) and not reported here for brevity (see Fig. 1). Contribution of the waste heat emissions from building heating ventilation and air conditioning (HVAC) system $\mathrm{S_{\Theta waste}}$ is parameterized by

$$S_{\Theta waste} = F_{st}\frac{1}{\rho C_p \Delta z}Q_{HVAC}, \tag{13}$$

where $\mathrm{Q_{HVAC}}$ is total sensible waste heat released into the urban atmosphere per building footprint area, $\mathrm{F_{st}}$ is the fraction of waste heat released at street level, while the remainder fraction $1-\mathrm{F_{st}}$ is released at roof level, and $\Delta\mathrm{z}$ is grid discretization in the vertical direction. Depending on the type of building, waste heat emissions can be released partially at street level and the rest at roof level, which can be adjusted by changing $\mathrm{F_{st}}$ from 0 to 1. In this study, it is set to 0.3. Term $\mathrm{Q_{HVAC}}$ is calculated by the building energy model as

$$Q_{HVAC} = \underbrace{\underbrace{Q_{surf} + Q_{ven} + Q_{inf} + Q_{int}}_{Q_{cool}} + W_{cool}}_{\text{Cooling waste heat}} + Q_{dehum} + Q_{gas} + Q_{water}, \tag{14}$$

$$Q_{HVAC} = \underbrace{\underbrace{(Q_{surf} + Q_{ven} + Q_{inf} + Q_{int})}_{Q_{heat}}/\eta_{heat}}_{\text{Heating waste heat}} + Q_{dehum} + Q_{gas} + Q_{water}, \tag{15}$$

under cooling and heating mode, respectively. Under cooling mode $\mathrm{Q_{HVAC}}$ is calculated by adding the cooling demand (Q_{cool}), consisting of surface cooling demand, ventilation demand, infiltration (or exfiltration) demand, and internal energy demand (lighting, equipment, and occupants), energy consumption of the cooling system (W_{cool}), dehumidification demand (Q_{dehum}), energy consumption by gas combustion (e.g. cooking) (Q_{gas}), and energy consumption for water heating (Q_{water}). Under heating mode, $\mathrm{Q_{HVAC}}$ is calculated by adding the heating waste heat (Q_{heat}), consisting of surface heating demand, ventilation demand, infiltration (or exfiltration) demand, and internal energy demand (lighting, equipment, and occupants) (accounting for thermal efficiency of the heating system (η_{heat})), dehumidification demand (Q_{dehum}), energy consumption by gas combustion (e.g. cooking) (Q_{gas}), and energy consumption for water heating (Q_{water}).

To complete the urban one-dimensional vertical diffusion model (see Fig. 1), the transport equation for specific humidity is

$$\frac{\partial \overline{Q}}{\partial t} = \underbrace{\frac{\partial}{\partial z}\left(\frac{K_m}{Sc_t}\frac{\partial \overline{Q}}{\partial z}\right)}_{I} + \underbrace{S_{QV}}_{II}, \tag{16}$$

where $\overline{\mathrm{Q}}$ is time-averaged specific humidity. The turbulent transport of specific humidity (I) is parameterized based on K-theory, $\mathrm{Sc_t}$ is turbulent Schmidt number set to 1 in this study, and source term $\mathrm{S_{QV}}$ (II) is caused by latent heat from vegetation detailed in appendix A and by Krayenhoff (2014) but not reported here for brevity.

2.1.4 Building Energy Model

In this study, the balance equation for convection, conduction, and radiation heat fluxes is applied to all building elements (wall, roof, floor, windows, ceiling, and internal mass) to calculate the indoor air temperature. Then, a sensible heat balance equation, between convective heat fluxes released from indoor surfaces and internal heat gains and sensible heat fluxes from HVAC system and infiltration (or exfiltration), is solved to obtain the time evolution of indoor temperature as

$$\forall \rho C_p \frac{dT_{in}}{dt} = \underbrace{Q_{surf} + Q_{ven} + Q_{inf} + Q_{int}}_{Q_{cool/heat}}, \tag{17}$$

where $\forall$ is indoor volume, $\mathrm{T_{in}}$ is indoor air temperature, and $\mathrm{Q_{cool/heat}}$ is cooling or heating demand as specified in Eqs. 14 and 15. More details on parameterization of the terms in Eq. 17 can be found in appendix A and Bueno et al. (2012b) but are not reported here for brevity.

A similar balance equation can be derived for latent heat to determine the time evolution of the indoor air specific humidity as well as the dehumidification load Q_{dehum}, which is parameterized in Bueno et al. (2012b) but is not detailed here for brevity. Note that energy consumption by gas combustion (e.g. cooking) Q_{gas} and water heating Q_{water} does not influence indoor air temperature or specific humidity, but such energy consumption sources appear in the waste heat Eqs. 14 and 15. These terms are determined from schedules (Bueno et al., 2012b).

2.1.5 Radiation Model with Vegetation

In VCWG, there are two types of vegetation: ground vegetation cover and trees. Ground vegetation cover fraction is specified by δ_{s}. Tree vegetation is specified by four parameters: Leaf Area Index (LAI), Leaf Area Density (LAD) profile, cover fraction of tree canopy δ_t, and trunk height h_t. Both types of vegetation are specified with the same albedo α_V and emissivity ε_V. The VCWG user can change these input parameters for different vegetation structures. The parameterization of shortwave radiation accounts for the incoming direct and diffuse components of solar radiation, and it is used in this study to account for the shading effects of trees on vertical and horizontal urban surfaces as well as the shading effect of buildings on trees. The total amount of shortwave radiation absorbed by each urban element S_i is calculated by adding the before-reflection absorption of shortwave radiation to the sum of multiple reflections within the canyon (Redon et al., 2017). Parameterization of the longwave radiation received and emitted by the urban elements L_i assumes Lambertian surfaces. Again the total amount of longwave radiation absorbed by each urban element is calculated by adding the before-reflection absorption of longwave radiation to the sum of multiple reflections within the canyon (Loughner et al., 2012). Both shortwave and longwave radiation models are coupled to the vertical diffusion and the building energy models using feedback interaction. Detailed formulations are not provided here for brevity, but the reader is referred to the appendix A and original studies by Redon et al. (2017) and Loughner et al. (2012).

2.2 Experimental Field Campaign

2.2.1 Logistics

To evaluate results from VCWG, comprehensive microclimate field measurements were conducted from 15 July 2018 to 5 September 2018, in Guelph, Canada, which is detailed below. Guelph is located in southwestern Ontario, Canada, with cold Winters and humid Summers. The urban microclimate field measurements were conducted in the Reek Walk, a typical quasi two-dimensional urban canyon, located at the University of Guelph (43.5323°N and 80.2253°W). The rural microclimate field measurements were conducted in the Guelph Turfgrass Institute, a research green space area located at 43.5473°N and 80.2149°W, about 2 km northeast of the Reek Walk (see Fig. 3). The average building height for the urban area is H_{avg}=20 m, and the plan area density is λ_p=0.55. The road, Reek Walk, where meteorological instruments were installed, is covered by grass and asphalt in equal fractions. As shown in Fig. 3, urban trees are distributed across the neighbourhood.

The urban canyon axis is oriented in the northwest-southeast direction and x and y directions are set to be cross- and the along-canyon, respectively (see Fig. 4). The frontal area density λ_f varies from 0.31 to 0.51 when the approaching wind direction changes from along- to cross-canyon, respectively. Figure 4 shows that the predominant wind directions were from west and southwest, roughly perpendicular to the canyon axis, for the field campaign duration. Based on studies aimed to characterize the wind flow pattern within a built-up area (Zajic et al., 2011; Grimmond and Oke, 1999), the observed flow configuration alternates between skimming flow and wake interface regimes. However, the flow within the urban site is more complicated than the simple regimes and the associated parametrizations.

2.2.2 Instruments

In the rural site, wind speed, wind direction (at 10 m elevation), relative humidity, and temperature (at 2 m elevation) are collected on an hourly basis by the Guelph Turfgrass Institute meteorological station, which bears World Meteorological Organization (WMO) identifier 71833. Data from this station and those of EPW for London, Ontario, were combined to create

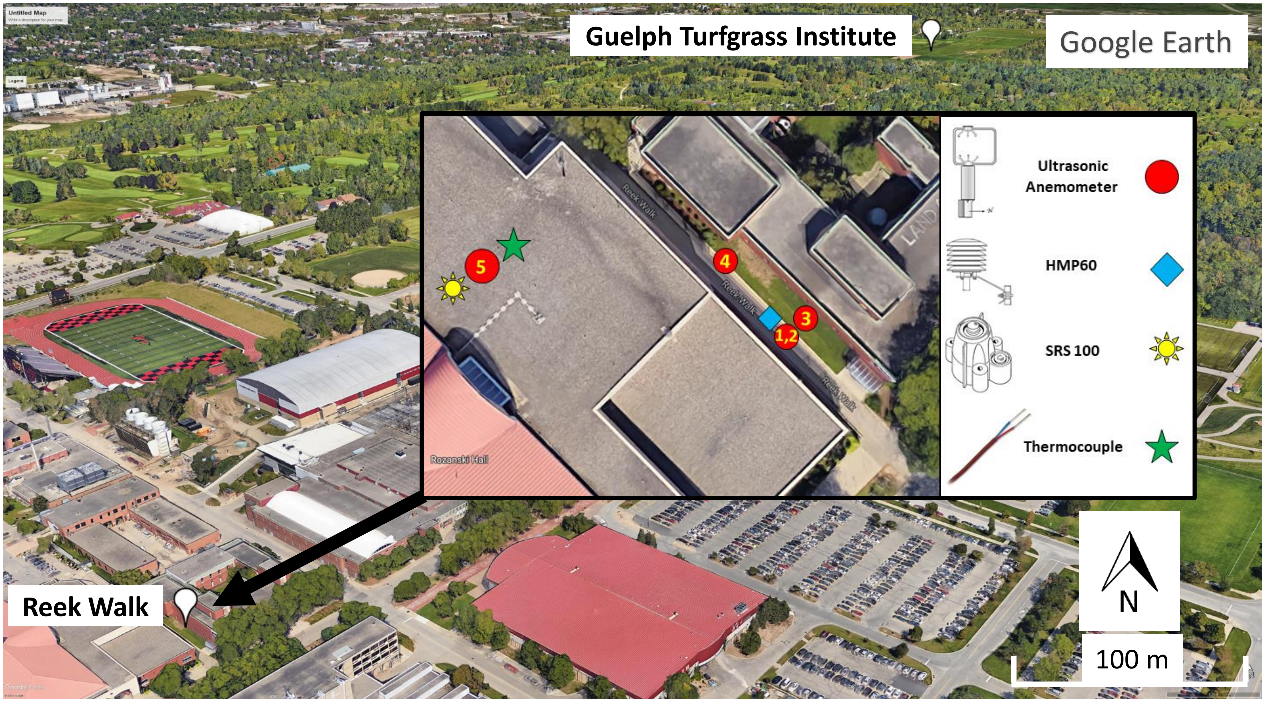

Figure 3. View of the rural weather station (Guelph Turfgrass Institute) and the urban site (Reek Walk, University of Guelph) used for the microclimate field campaign; inset map shows the location of the meteorological instruments in the urban site; images were obtained from Google Earth.

an EPW dataset for model evaluation. In the urban site, meteorological data was collected within and above the canyon using five 81000 R. M. Young ultrasonic anemometers from Young U.S.A.[2] distributed horizontally and vertically. The accuracy and resolution of measurements for wind speed were $\pm 1\%$ and 0.01 $\mathrm{m\,s^{-1}}$, respectively, and for temperature were ± 2 K and 0.01 K, respectively. Four anemometers were deployed within the canyon, two were placed on a pole at heights of 2.4 m and 5.5 m elevation from the ground and the other two anemometers were located 4 m and 30 m away from the pole in the cross- and along-canyon directions, respectively. The fifth anemometer was deployed on a tripod on the roof at 2.5 m elevation from roof level (see Fig. 3). Three of these anemometers located at different elevations were used for comparison to VCWG model results. It has been suggested that the sampling frequency should be at least 10 Hz to measure atmospheric turbulence (Balogun et al., 2010; Giometto et al., 2016; Aliabadi et al., 2019). The anemometers were adjusted to sample three components of wind speed and air temperature at a frequency of 20 Hz using Campbell Scientific[3] CR6 data loggers. As shown in Fig. 3, a Campbell

[2]http://youngusa.com/
[3]https://www.campbellsci.ca

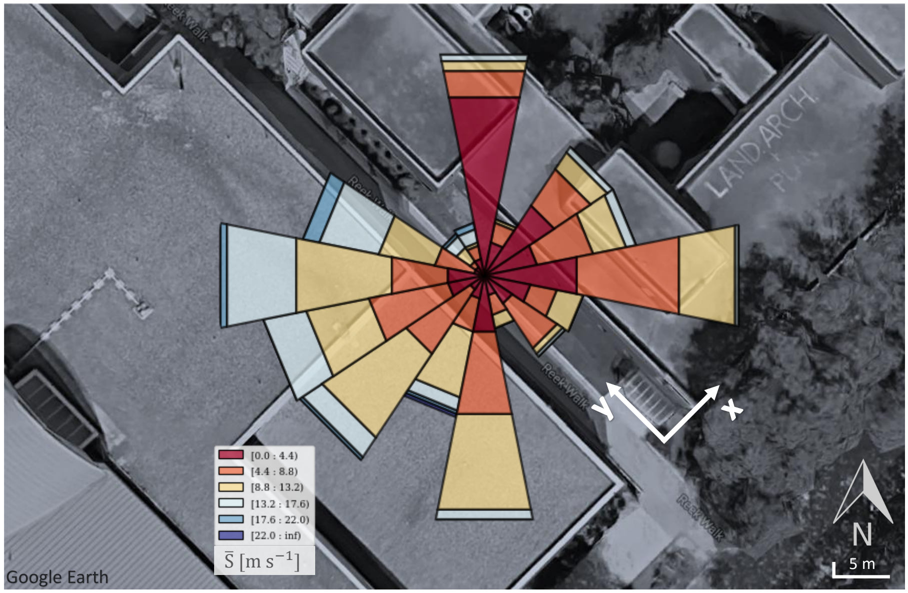

Figure 4. Wind rose plot above the urban site (Reek Walk, University of Guelph) between 15 July 2018 and 5 September 2018; image was obtained from Google Earth.

Scientific HMP60 sensor was deployed at 1 m elevation, which measured minute-averaged relative humidity with an accuracy of $\pm 3\%$ and temperature with an accuracy of $\pm 0.6\mathrm{K}$.

Wind tunnel tests were conducted to calibrate the wind speeds measured by the ultrasonic anemometers against a reference pitot tube (No figures are shown for this calibration). The HMP60 sensor was used as the reference measurement to calibrate all other temperatures and relative humidities measured, including those of the WMO station.

3 Results and Discussion

In this section, the VCWG model results are compared to the microclimate field measurements. We also explored the capability of the model to predict urban climate for investigations of the effects of building dimensions, urban vegetation, building energy configuration, radiation configuration, seasonal variations, and other climates. The simplified urban neighbourhood is depicted in Fig. 2. In VCWG, buildings with uniformly-distributed height, equal width, and equal spacing from one another, represent the urban area. The computational domain height is five times the average building height, which makes it suitable for microclimate analysis (Santiago and Martilli, 2010; Aliabadi et al., 2017). A uniform Cartesian grid with 2 m vertical resolution is used, where buildings are removed from control volumes (see Fig. 2). The flow is assumed to be pressure-driven with the pressure gradient of $\rho \mathrm{u}_*^2/\mathrm{H}_{\mathrm{top}}$, which is decomposed into the x and y directions based on the wind angle. In this equation, the adjustment for wind angle is made based on canyon orientation and the incoming wind angle at the top of the domain. This pressure gradient is forced as source terms on the momentum Eqs. 8 and 9. The boundary condition for potential

Table 1. List of input parameters used to run VCWG for model evaluation.

Parameter	Symbol	Value
Latitude °N	lat	43.53
Longitude °W	lon	80.22
Season	-	Summer
Plan area density	λ_{p}	0.44
Frontal area density	λ_{f}	0.55
Average buildings height [m]	$\mathrm{H_{avg}}$	20
Average of leaf area density profile $[\mathrm{m^2 m^{-3}}]$	LAD	0.28
Trunk height [m]	$\mathrm{h_t}$	4
Cover fraction of tree canopy	δ_{t}	0.48
Ground vegetation cover fraction	δ_{s}	0.5
Building type	-	Office
Urban albedos (roof, ground, wall, vegetation)	$\alpha_{\mathrm{R}}, \alpha_{\mathrm{G}}, \alpha_{\mathrm{W}}, \alpha_{\mathrm{V}}$	0.22, 0.08, 0.2, 0.2
Urban emissivities (roof, ground, wall, vegetation)	$\varepsilon_{\mathrm{R}}, \varepsilon_{\mathrm{G}}, \varepsilon_{\mathrm{W}}, \varepsilon_{\mathrm{V}}$	0.9, 0.94, 0.9, 0.95
Rural overall albedo	α_{rur}	0.2
Rural overall emissivity	$\varepsilon_{\mathrm{rur}}$	0.93
Rural aerodynamic roughness length [m]	$\mathrm{z_{0rur}}$	0.1
Ground aerodynamic roughness length [m]	$\mathrm{z_{0G}}$	0.02
Roof aerodynamic roughness length [m]	$\mathrm{z_{0R}}$	0.02
Vertical resolution [m]	$\Delta\mathrm{z}$	2
Time step [s]	$\Delta\mathrm{t}$	60
Canyon axis orientation °N	θ_{can}	-45

temperature and humidity equations (Eqs. 12 and 16) are determined from the rural model (see Fig. 1). Thus, the VCWG is aimed to calculate momentum and energy exchanges for the centre of each cell in the vertical direction based on the boundary conditions obtained from the rural model, the building energy model, and the radiation model.

3.1 Model-Observation Comparison

The results of the VCWG are now compared to the measured data collected during the microclimate field campaign. The actual weather data in the rural area including wind speed and wind direction at $10\ \mathrm{m}$ elevation, temperature and relative humidity at $2\ \mathrm{m}$ elevation, atmospheric pressure, and terms describing radiative fluxes are used from the assembled EPW dataset. The input parameters representing the urban area are listed in Table 1. The simulations were run for two weeks starting from 15 August 2018 with the first 24 hours treated as model spin-up period. For such analysis, the run time is approximately 15 minutes, however it can vary slightly depending on the grid spacing and time step.

To compare VCWG results with measured meteorological variables from field campaign, the hourly BIAS and Root Mean Square Error (RMSE) are calculated over an entire diurnal cycle by considering the model results and measurements over a two-week period. These statistics are calculated for potential temperature at different heights, wind speed at different heights, and specific humidity near the ground. For the Urban Heat Island (UHI) the overall mean and standard deviation is calculated. BIAS and RMSE are defined as

$$BIAS = \frac{\sum_{i=1}^{n}(M_i - O_i)}{n}, \tag{18}$$

$$RMSE = \sqrt{\frac{\sum_{i=1}^{n}(M_i - O_i)^2}{n}}, \tag{19}$$

where $\mathrm{M_i}$ and $\mathrm{O_i}$ are modelled and measured (observed) quantities. Here n is 14 because each hourly model-observation comparison is conduced over two weeks.

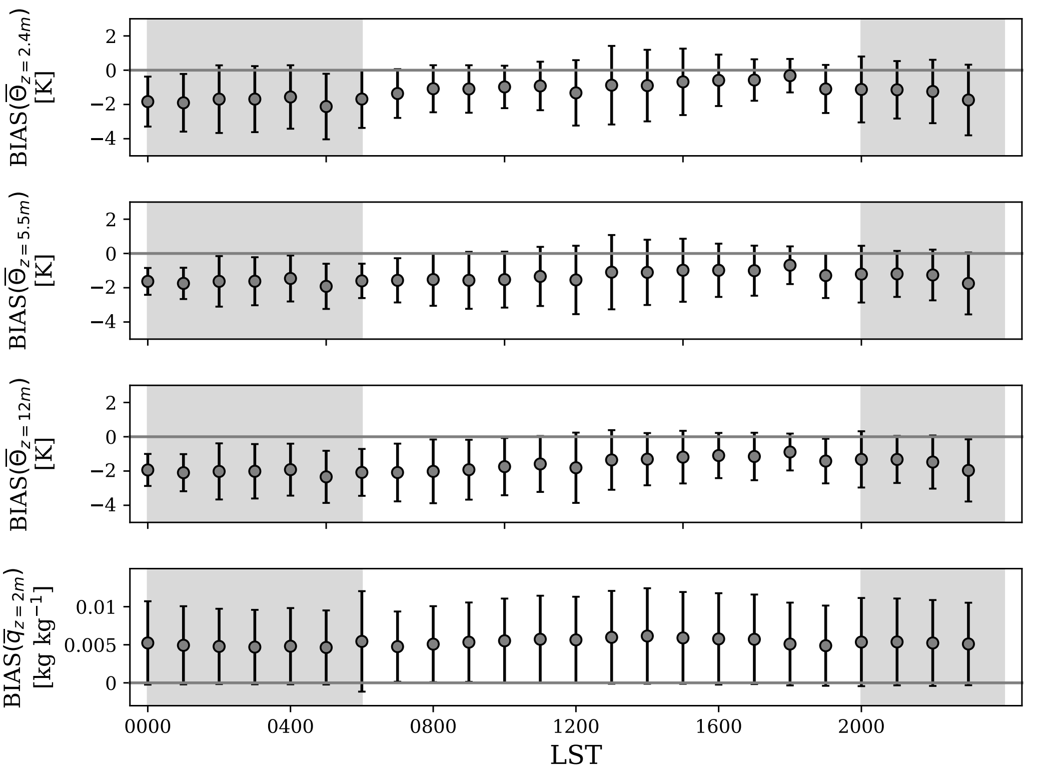

Figure 5. Comparison between the field measurements and the VCWG prediction of potential temperature (at various elevations) and specific humidity near the ground in the urban site; diurnal variation of BIAS and RMSE (error bar) are shown using data obtained over a two-week period; nighttime is shown with shaded regions; times in Local Standard Time (LST).

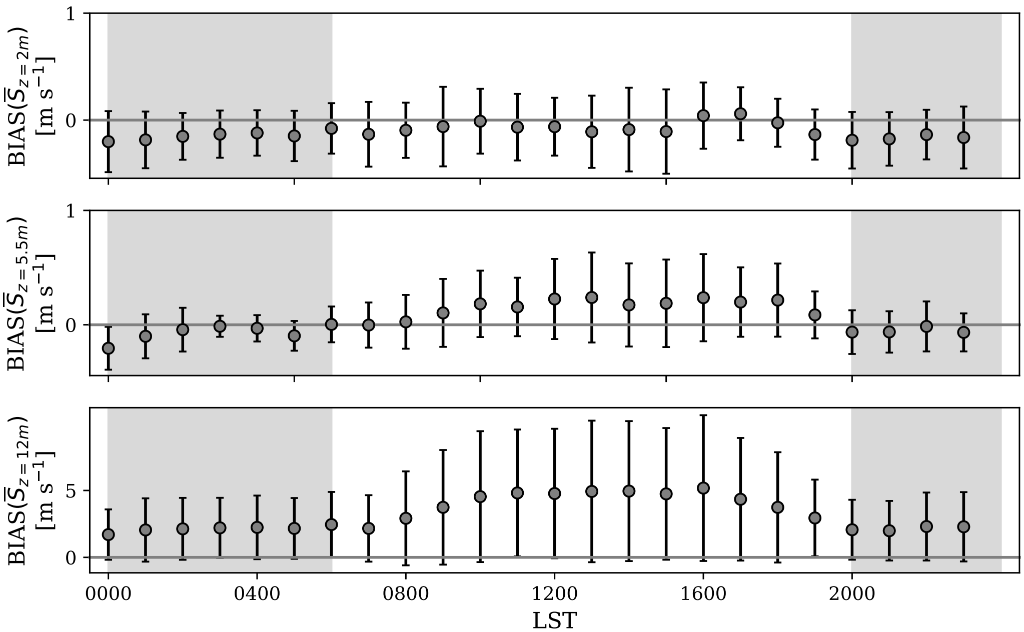

Figure 6. Comparison between the field measurements and the VCWG prediction of wind speed (at various elevations) in the urban site; diurnal variation of BIAS and RMSE (error bar) are shown using data obtained over a two-week period; nighttime is shown with shaded regions; times in Local Standard Time (LST).

The error statistics are shown in Figs. 5 and 6. The average BIAS and RMSE for temperature are -1.43 and 1.56 K, respectively. It can be seen that the hourly BIAS is within 2 K and the model exhibits a cold BIAS most of the time with respect to the observations. The average BIAS and RMSE for specific humidity are 0.005 and 0.006 kgkg^{-1}, respectively. It can be seen that the hourly BIAS is within 0.005 kgkg^{-1} and the model exhibits a positive BIAS most of the time with respect to the observations.

The average BIAS and RMSE for wind speed are 1.06 and 1.32 ms^{-1}, respectively. It can be seen that the hourly BIAS is within 0.5 ms^{-1} at 2 and 5.5 m elevations, which indicates that at these elevations the effects of urban obstacles inducing drag and reducing wind speed within the built-up area are captured well by the model. However, the BIAS is higher at 12 m elevation. Here VCWG exhibits a positive hourly BIAS up to 5 ms^{-1} during windy conditions in the mid afternoon period. It has been proposed that the oncoming boundary layer and the shear layer developing at the roof level significantly contribute in mass and momentum exchange between the in-canyon and above-canyon atmosphere (Kang and Sung, 2009; Perret and Savory, 2013). This shear layer is characterized by highly turbulent flow making realistic modeling more challenging (Salizzoni et al., 2011; Perret and Savory, 2013) thus explaining the model deviation from the observations at higher elevations closer to the shear layer.

UHI for the observation is computed by considering the difference between the average temperature measurements inside the canyon and those temperatures provided by the EPW dataset. For VCWG, UHI is calculated by considering the difference between the average temperature prediction in the canyon from 2 m to average building height elevation and the average temperature prediction using the rural model for the same range of elevations. The average VCWG-predicted mean and standard deviation for UHI are $+1.20$ and 1.53 K, respectively. These values are in reasonable agreement with observations reporting mean and standard deviation for UHI of $+1.08$ and 1.23 K, respectively.

3.2 Model Exploration

The VCWG performance is assessed by evaluating the model performance as a function of the urban configurations ($\lambda_\mathrm{p}, \lambda_\mathrm{f}$, LAD), building energy configuration (building type, thermal efficiency, and coefficient of performance), radiation configuration (canyon aspect ratio and canyon axis angle), different seasons, different climate zones, and time series analysis. Except for the analysis of different seasons and climate zones, all explorations were performed by running VCWG to simulate the urban microclimate in Vancouver, Canada, for two weeks in August 2011. For exploration of different seasons, VCWG was run to simulate the urban microclimate in Vancouver, Canada, for an entire year in 2011. For different climate zones, VCWG was run to simulate the urban microclimate in other cities. More details on the explorations are provided in the subsequent sections. Such analyses will provide more information on spatiotemporal variation of the atmospheric meteorological variables and reveal the complexity of urban microclimate modeling. Additionally, the potentials and limitations of VCWG will be discussed.

3.2.1 Urban Plan and Frontal Area Densities

In urban canopy modeling, two parameters often used to describe building and canyon geometries are plan area density (λ_p), which is the ratio of the total plan area of the buildings to the total urban flat-earth surface area, and the frontal area density (λ_f), which is the ratio of the total frontal area (facing wind) to the total urban flat-earth surface area. An urban area can be characterized with different types of land use, where each type may have different plan and frontal area densities, they can vary from high values in industrial districts to low values associated with the land used for public transportation (Wong et al., 2010). Most development in an urban area could be associated with changing λ_p and λ_f, which can alter the local climate in different ways such as air and surface temperatures, building energy consumption, and thermal and wind comfort levels (Coutts et al., 2007; Emmanuel and Steemers, 2018).

Two case studies λ_p=0.36 and 0.56 are explored to assess the model and see how the urban microclimate changes when the plan area density increases while keeping the other parameters unchanged. Figure 7 shows typical nighttime and daytime profiles of potential temperature and mean horizontal wind speed in the urban area associated with running the model for one day. Higher λ_p is associated with more urban surfaces allowing greater absorption of longwave and shortwave radiation and therefore higher level of building energy consumption for cooling (or heating). It is depicted in Fig. 7 that the case with higher λ_p shows higher potential temperature profiles during the day and night. During the nighttime, the temperature difference between the cases is not as much as the daytime, however, still higher temperatures can be obtained when plan area density is higher. Additionally, more urban surfaces impose more drag and consequently reduce wind speed (see Fig. 7).

Further investigations are performed for different frontal area densities λ_f= 0.55 and 0.84 by running the model for one day. At first glance, the cities with high-rise buildings are supposed to release more heat into the outdoor environment due to greater urban surfaces, but tall buildings can provide solar shading during the daytime and decrease temperature of the surfaces. As shown in Fig. 8, any increase in λ_f reduces potential temperature in the urban area during the day. However, due to the lack of shortwave radiation over nighttime and that urban surfaces are the main source of heat that can be released into the atmosphere, higher λ_f results in higher potential temperatures at nighttime due to radiation trapping. Moreover, increasing frontal area density tends to increase surface roughness and consequently slow down wind speed within the canyon during daytime, which can also be depicted in Fig. 8.

The VCWG results are also consistent with previous studies in the literature (Coutts et al., 2007; Zajic et al., 2011; Santiago et al., 2014). The findings reported here highlight the careful considerations that need to be accounted for by city planners.

3.2.2 Leaf Area Density

Urban trees interact with the other urban elements by providing shade to reduce temperature of surfaces, removing the stored heat in the canyon substantially, and induce drag to reduce wind speed (Loughner et al., 2012; Krayenhoff et al., 2015; Redon et al., 2017). The capability of the VCWG to take into account these effects is assessed by investigating two case studies with LAD representing trees with average foliage densities of 0.08 and 0.14 $\mathrm{m^2m^{-3}}$, respectively, by running the model for one day. The result is shown in Fig. 9. The cooling effect of the trees is evident when the average LAD of tree foliage increases, resulting in a decrease of potential temperature within the canyon, particularly during the day when the shading effect of trees lowers the surface temperatures. Such effects not only can improve thermal comfort at the pedestrian level, but also reduce the building energy consumption in the Summertime (Souch and Souch, 1993; Akbari et al., 2001). On the other hand, the urban trees are thought to be a sink of momentum and kinetic energy by exerting drag and damping the flow fluctuations (Giometto et al., 2017; Yuan et al., 2017). This effect cannot be modeled very well by VCWG, which predicts the same level of wind speed within the canyon at the two LAD profiles. The analysis obtained from this exploration is in reasonable agreement with previous works (Souch and Souch, 1993; Loughner et al., 2012; Giometto et al., 2017; Yuan et al., 2017). Trees are recognized to be essential urban elements to moderate extreme wind speeds and heat waves, particularly during the warm season.

3.2.3 Building Energy Configuration

The building energy model within VCWG is explored by running VCWG under different building types, cooling system Coefficient Of Performance (COP), and heating system thermal efficiency η_heat. Two building types are considered, a school and a small office, with specifications provided in Table 2. It can be noted that the infiltration rate, ventilation rate, volumetric flow for water heating, and waste heat fluxes associated with gas combustion, electricity consumption, and lighting for a school are substantially greater than those for a small office. Note that construction material properties are also different for a school and small office within VCWG schedules, but the differences are not specified here for brevity. Two sets of COP and

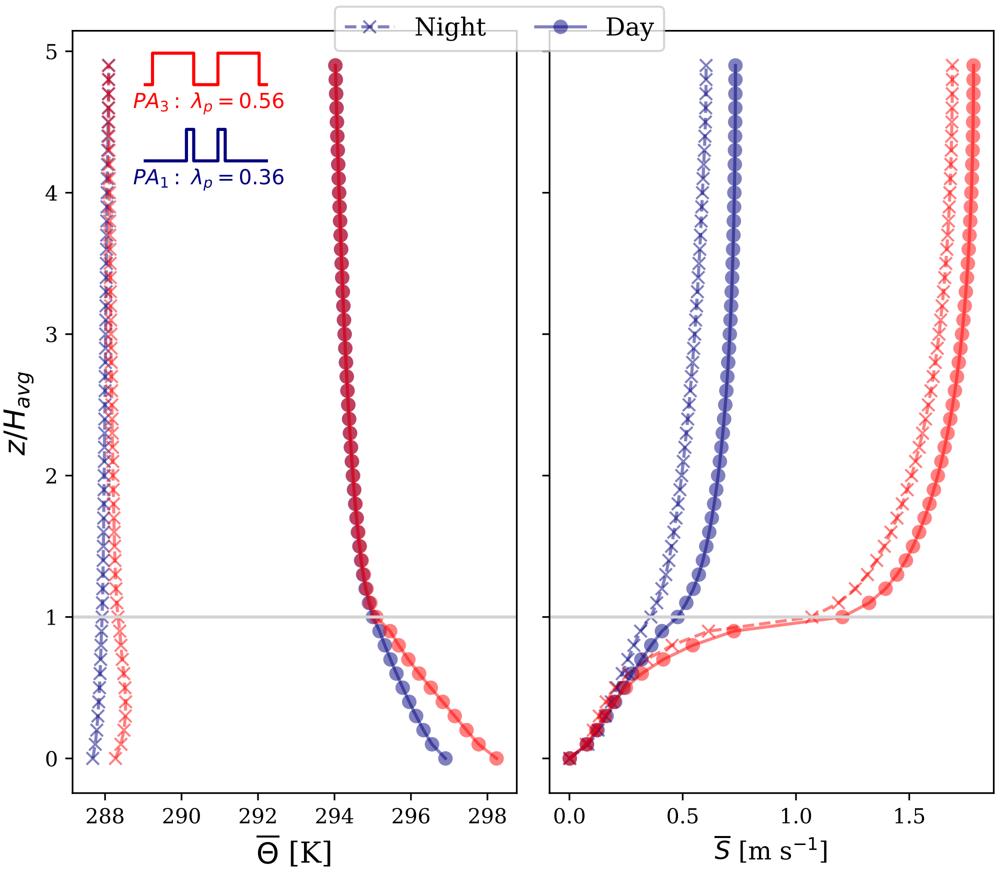

Figure 7. Effect of plan area density λ_p on the profiles of potential temperature and mean horizontal wind speed during nighttime (averaged from 0000 to 0400 LST) and daytime (averaged from 1200 to 1600 LST).

η_heat are considered for a small office. For an energy-efficient building values COP=3 and η_heat=0.8 are used, while for a low-energy-efficient building values COP=1 and η_heat=0.4 are used.

Figure 10 shows the effect of building type on hourly mean and standard deviation of cooling/heating waste heat, dehumidification waste heat, gas combustion waste heat, water heating waste heat, and UHI calculated for running the model for two weeks. The waste heat fluxes are reported per unit building footprint area. It can be noted that the building energy system operates under heating mode for a few hours around sunrise, while it runs under cooling mode for the majority of daytime period. It can be noted that a school results in higher values of waste heats and UHI, so the potential impact of an energy-intensive school on the urban climate may be higher than a small office. It is noted that a school generates substantial waste heat fluxes associated with gas combustion (due to cooking activities) and water heating (for domestic use) because of higher occupancy compared to a small office.

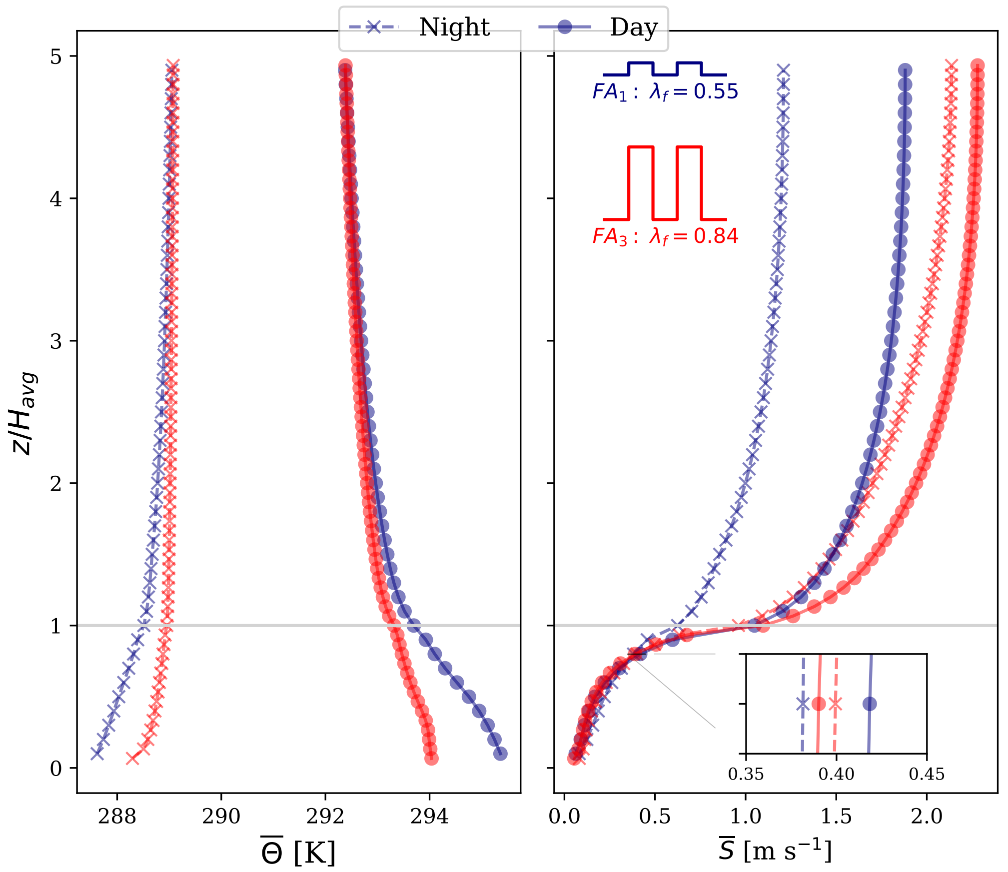

Figure 8. Effect of frontal area density λ_f on the profiles of potential temperature and mean horizontal wind speed during nighttime (averaged from 0000 to 0400 LST) and daytime (averaged from 1200 to 1600 LST).

Figure 11 shows the effect of building cooling system Coefficient Of Performance (COP) and heating system thermal efficiency (η_heat) on hourly mean and standard deviation of waste heats and UHI calculated for running the model for two weeks. It can be noted that lower COP and thermal efficiency result in higher values of waste heats and UHI, so the potential impact of an energy-intensive building on the urban climate may be higher than an energy-efficient building. Most particularly, it can be noted that lower heating system thermal efficiency results in greater waste heat flux for water heating.

3.2.4 Radiation Configuration

The radiation model within VCWG is explored by running VCWG under different canyon aspect ratios $\mathrm{H_{avg}/w}$ and different street canyon axis angles θ_can with respect to the north axis to investigates the effects on direct solar radiation, diffuse solar radiation, and longwave fluxes. For exploring the effect of canyon aspect ratio on these fluxes values of $\mathrm{H_{avg}/w}$=3 and 2 are

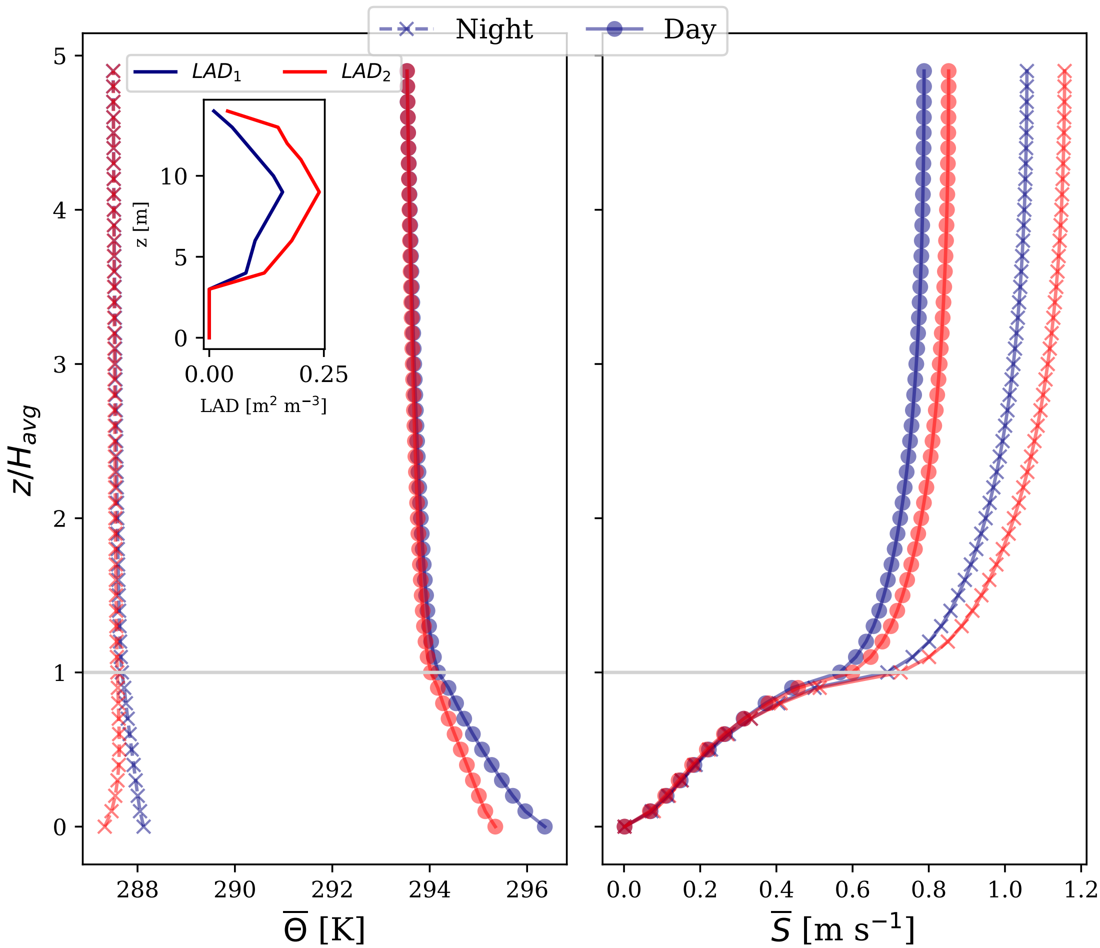

Figure 9. Effect of leaf area density profiles on the profiles of potential temperature and mean horizontal wind speed during nighttime (averaged from 0000 to 0400 LST) and daytime (averaged from 1200 to 1600 LST).

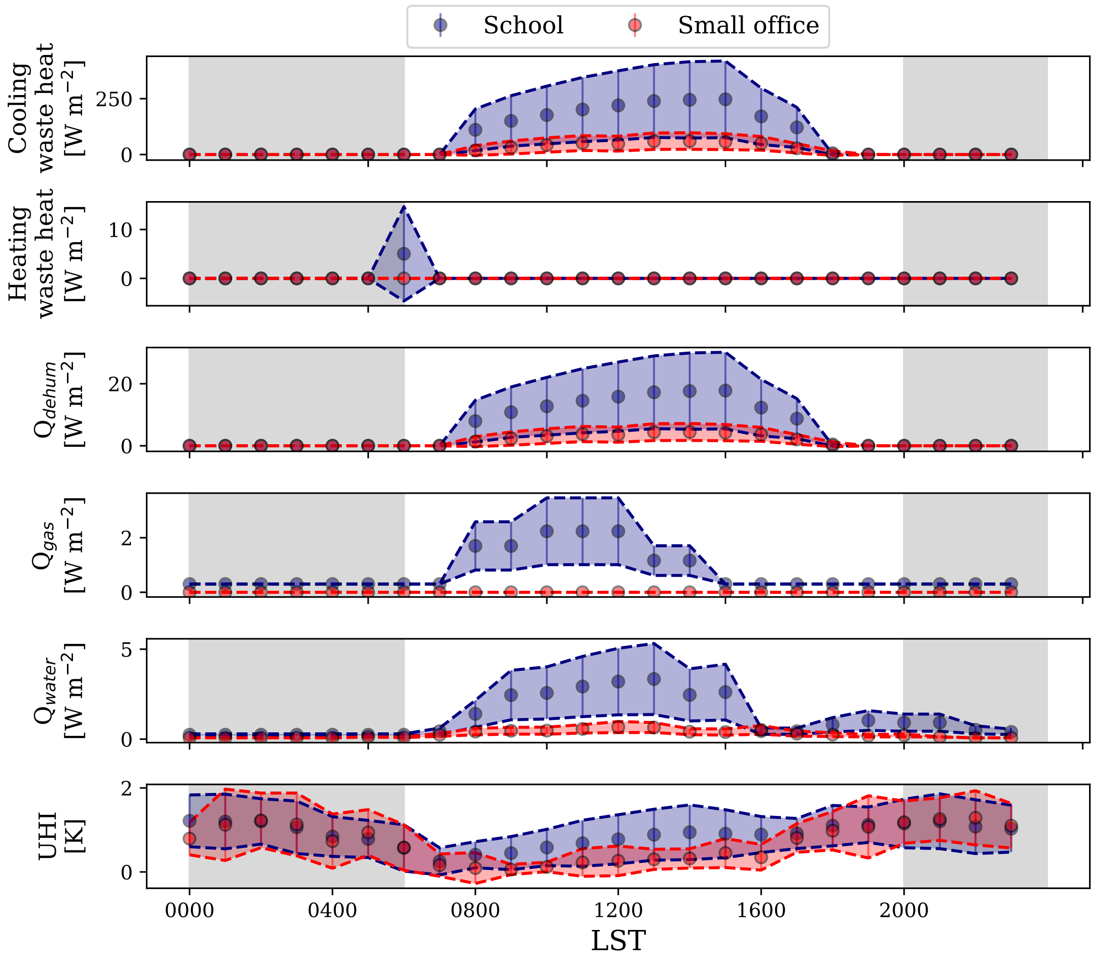

Figure 10. Effect of building type on cooling/heating waste heat, dehumidification waste heat, gas combustion waste heat, water heating waste heat, and UHI; diurnal variation of mean and standard variation (error bar) are shown using data obtained over a two-week period; nighttime is shown with shaded regions; times in Local Standard Time (LST).

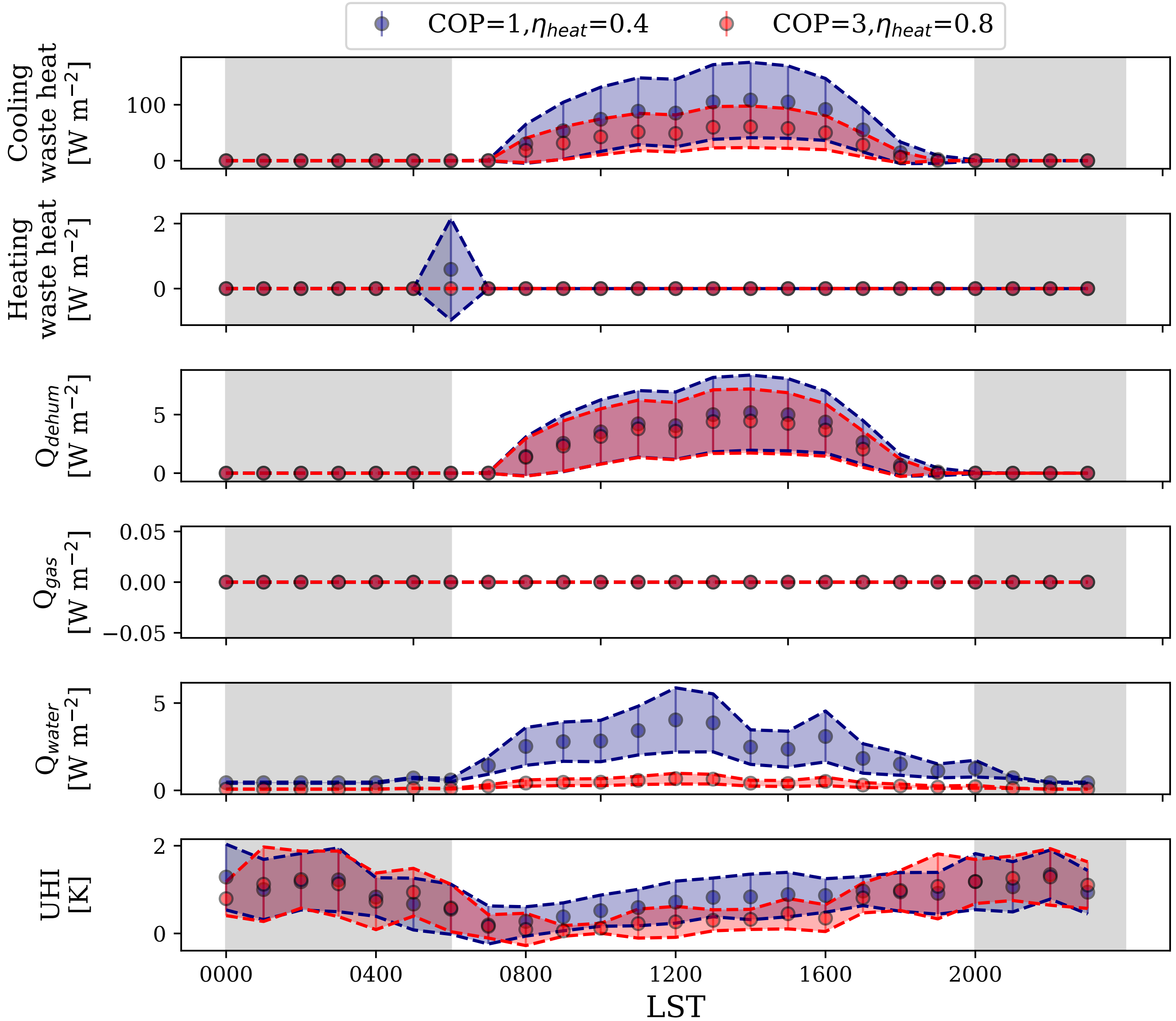

Figure 11. Effect of building cooling system Coefficient Of Performance (COP) and heating system thermal efficiency (η_{heat}) on cooling/heating waste heat, dehumidification waste heat, gas combustion waste heat, water heating waste heat, and UHI; diurnal variation of mean and standard variation (error bar) are shown using data obtained over a two-week period; nighttime is shown with shaded regions; times in Local Standard Time (LST).

Table 2. Specifications of the building energy configuration for two building types. The infiltration unit is Air Changes per Hour [ACH].

Building type → Building specification ↓	Small Office	School
COP	3.07	3.2
η_{heat}	0.8	0.75
Infiltration [ACH]	0.2	0.7
Ventilation [$\mathrm{Ls^{-1}}$]	275	55,583
Glazing ratio	0.21	0.34
Average volumetric flow for water heating [$\mathrm{Lh^{-1}}$]	11.4	161
Average waste heat flux from gas combustion [$\mathrm{Wm^{-2}}$]	0	0.617
Average waste heat flux from electricity consumption [$\mathrm{Wm^{-2}}$]	4	10.3
Average waste heat flux from lighting [$\mathrm{Wm^{-2}}$]	3.08	5.09

used with keeping θ_{can}=0 °, while for exploring the effect of street canyon axis angle on these fluxes values of θ_{can}=90 and 0 ° with respect to the north axis are used with keeping $\mathrm{H_{avg}/w}$=2. For these explorations VCWG is run for two weeks and hourly mean values for radiative fluxes are reported.

Figure 12 shows the radiative fluxes for different canyon aspect ratios. It can be seen that the direct solar radiation flux absorbed by the roof is not affected by the canyon aspect ratio, while the interior surfaces of the urban canyon absorb lower amounts of direct solar radiation flux for the higher canyon aspect ratio. This is expected since a higher canyon aspect ratio creates more shading effects on interior canyon surfaces compared to a lower canyon aspect ratio. Furthermore observe that the tree canopy receives slightly higher direct solar radiation flux compared to the road (consisting of ground and surface cover vegetation), for both canyon aspect ratios, because the tree canopy is at a higher elevation and more exposed to incoming direct solar radiation flux. Likewise, it can be seen that the diffuse solar radiation flux absorbed by the roof is not affected by the canyon aspect ratio, while the interior surfaces of the urban canyon absorb lower amounts of diffuse solar radiation flux for the higher canyon aspect ratio. Focusing on the net shortwave radiation flux components, i.e. the incoming shortwave radiation flux $\mathrm{S}^{\downarrow}$ and the outgoing shortwave radiation flux $\mathrm{S}^{\uparrow}$, it is noted that for the higher aspect ratio canyon the flux is more pronounced near noon Local Standard Time (LST), while for the lower aspect ratio canyon the flux is pronounced in more hours before and after noon LST. This expected since a higher aspect ratio canyon creates more shading effects on times before and after noon LST compared to a lower aspect ratio canyon. Focusing on the net longwave radiation flux components, i.e. the incoming longwave radiation flux $\mathrm{L}^{\downarrow}$ and the outgoing longwave radiation flux $\mathrm{L}^{\uparrow}$, it is noted that the canyon aspect ratio does not influence the radiation flux components substantially.

Figure 13 shows the radiative fluxes for different street canyon axis angles. It can be seen that the direct solar radiation flux absorbed by the roof is not affected by the street canyon axis angle, while the interior surfaces of the urban canyon show different responses to absorbing the direct solar radiation flux given the street canyon axis angle. With θ_{can}=90 ° the road

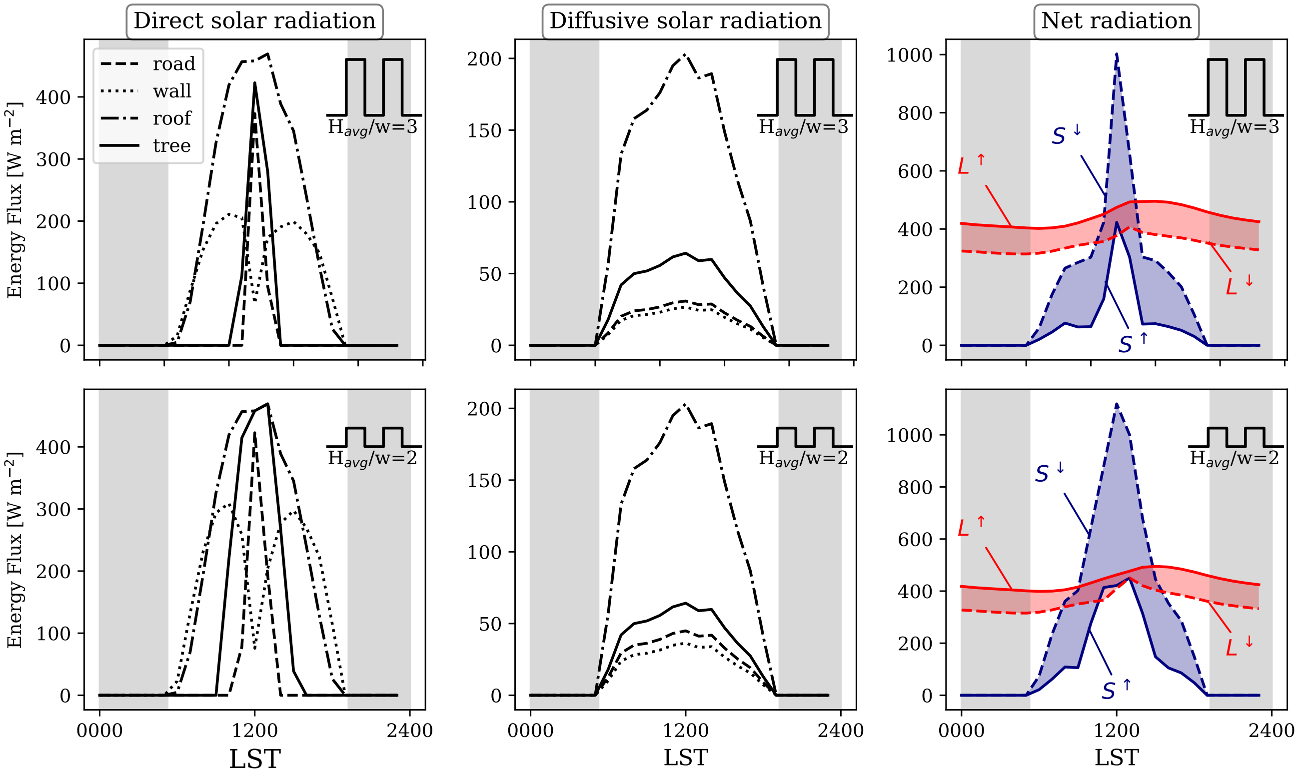

Figure 12. Effect of canyon aspect ratio $\mathrm{H_{avg}/w}$ on hourly mean direct solar radiation, diffuse solar radiation, and longwave radiation fluxes; diurnal variation of mean is shown using data obtained over a two-week period; nighttime is shown with shaded regions; times in Local Standard Time (LST).

surface absorbs the direct solar radiation flux in hours just after sunrise and before sunset, given that this flux reaches the road surface only at high solar zenith angles and solar azimuth angles from the east and west directions. On the other hand, with $\theta_{\mathrm{can}}=0\,^{\circ}$ the road surface absorbs the direct solar radiation flux in hours around noon LST, given that this flux reaches the road surface only at low solar zenith angles and solar azimuth angles from the north direction. Same trend can be observed for direct solar radiation flux absorbed by the tree canopy although the distribution is widened over more diurnal hours given the fact that the tree canopy is at a higher elevation and more exposed to incoming direct solar radiation flux compared to the road. With $\theta_{\mathrm{can}}=90\,^{\circ}$ the wall surface absorbs the direct solar radiation flux in most hours during midday, given that this flux reaches the wall surface with multiple combinations of solar zenith angles and solar azimuth angles. On the other hand, with $\theta_{\mathrm{can}}=0\,^{\circ}$ the wall surface absorbs little direct solar radiation flux in hours around noon LST, given that this flux does not reach the wall surface when the solar azimuth angle is from the north direction. In contrast, it can be seen that the diffuse solar radiation flux absorbed by all urban surfaces is not affected by the street canyon axis angle appreciably. Focusing on the net shortwave radiation flux components, the most notable difference is that the flux components are widened over a large range of diurnal hours when θ_{can}=90 ° due to the fact that multiple combinations of solar zenith and azimuth angles expose various urban surface to the incoming direct solar radiation flux. On the other hand when θ_{can}=0 ° the components of the shortwave radiation flux peak closer to noon LST and exhibit lower values after sunrise and before sunset hours since the combinations of solar zenith and azimuth angles do not expose interior canyon surfaces to the incoming direct solar radiation flux at those hours. Focusing on the net longwave radiation flux components, it is noted that the street canyon axis angle does not influence the radiation flux components substantially.

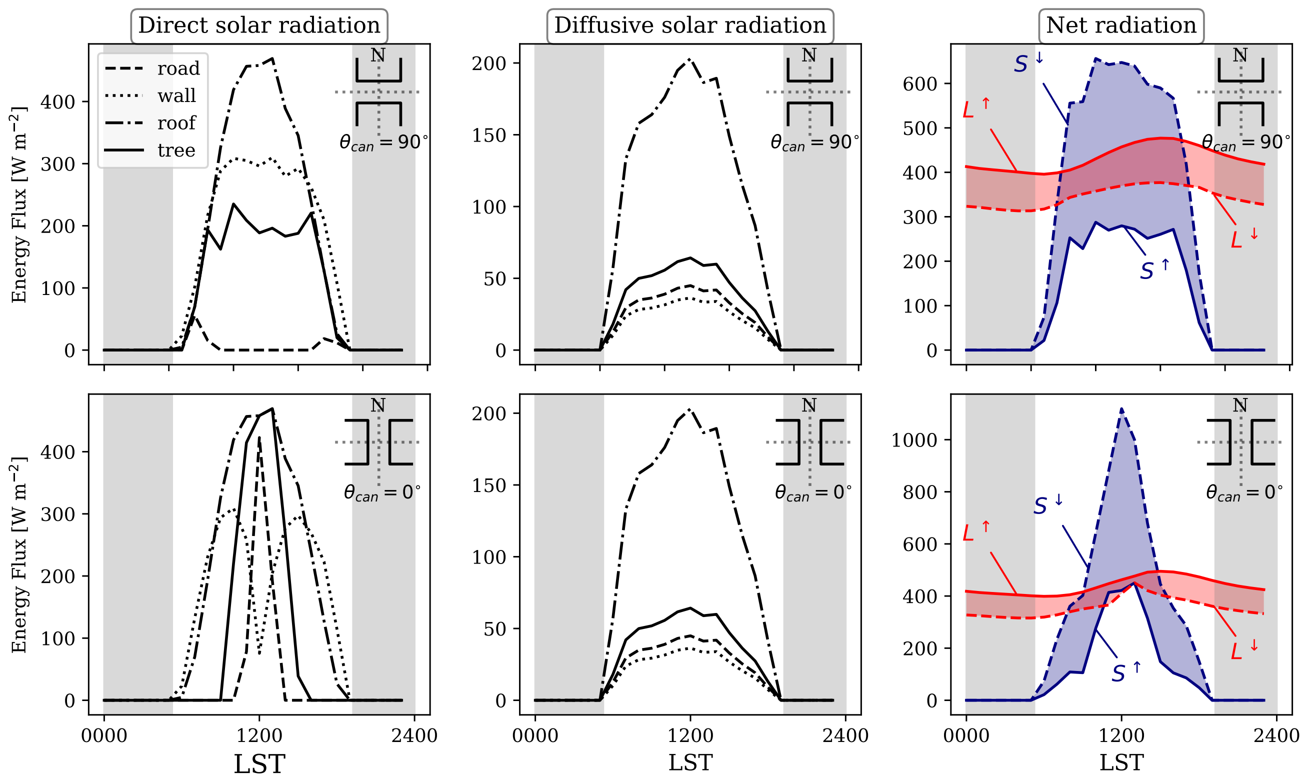

Figure 13. Effect of street canyon axis angle θ_{can} on hourly mean direct solar radiation, diffuse solar radiation, and longwave radiation fluxes; diurnal variation of mean is shown using data obtained over a two-week period; nighttime is shown with shaded regions; times in Local Standard Time (LST).

3.2.5 Seasonal Variations

In the context of urban development, there are no unique and pre-designed guidelines which can be extended to all built-up areas because careful considerations of geographical features and seasonal variations are required. For example, the type of urban vegetation, which is well suited for both warm and cold seasons in fulfilling thermal and wind comfort standards, can be climate specific (Jamei et al., 2016). Winter is characterized by larger zenith angles and lower solar radiation received by the surfaces compared to the other seasons. In Winter, the temperature difference between indoor and outdoor environment is higher than the Summer, thus, seasonal variations can alter building energy consumption and UHI effects substantially (Bueno et al., 2011). Figure 14 shows the VCWG results for the hourly mean values of UHI in each month of the year 2011 in Vancouver, Canada. In this exploration LAD is kept constant for all the months of the year. It can be noted that in general daytime UHI values are lower than nighttime values, as expected. Given the moderate climate of Vancouver, other than diurnal timing of UHI, no substantial change in the magnitude of UHI is predicted for different months of the year. The seasonal variation of UHI as predicted by VCWG is in agreement with a similar map reported by Oke et al. (2017).

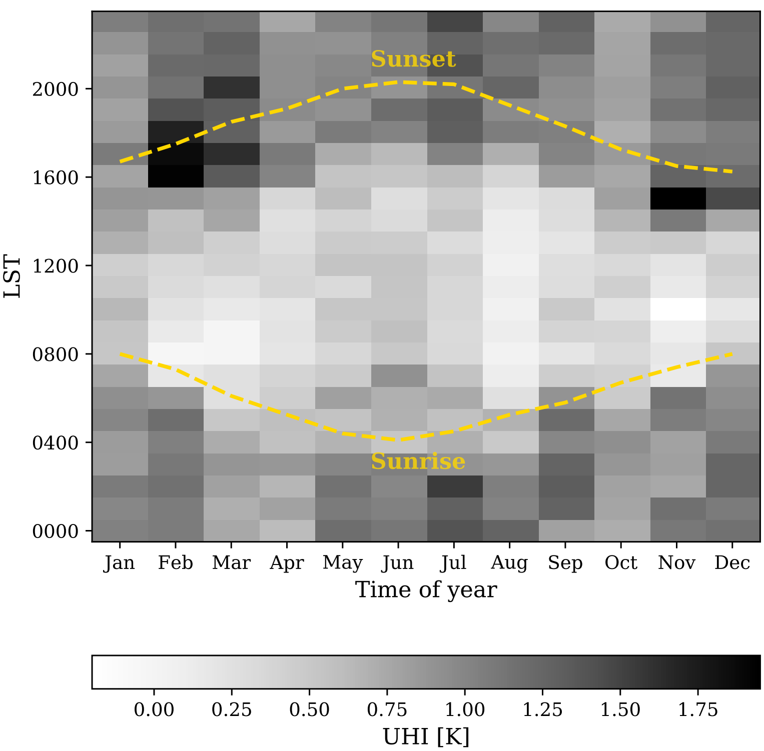

Figure 14. Hourly mean values of UHI in each month in Vancouver, Canada, as predicted by VCWG; sunrise and sunset times are denoted by dashed lines.

3.2.6 Other Climates

The VCWG was further explored by predicting UHI in different cities with different climate zones including Buenos Aires in January 1988, a city in the southern hemisphere with hot and humid climate, Phoenix in August 1980, which has a dry desert climate, Vancouver in August 2011, representing a moderate oceanic climate, Osaka in August 1996, with subtropical climate, and Copenhagen in August 1999, representing cold and temperate climate. All simulations were conducted for two weeks and then mean and standard variation of diurnal variations in UHI were calculated (see Fig. 15).

The result shows a diurnally-averaged value of $+1.0$ K for UHI for Buenos Aires, which is consistent with a previous study measuring a diurnally-averaged UHI of $+1.3$ K (Bejarán and Camilloni, 2003). The temperature difference between rural and urban areas in a dry and hot climate like Phoenix is relatively higher with the diurnally-averaged UHI value of $+2.4$ K, in agreement with a study measuring a diurnally-averaged UHI of $+2.5$ K (Hawkins et al., 2004; Fast et al., 2005). In case of Vancouver, the VCWG predicted a diurnally-averaged value of $+0.7$ K for UHI and showed high intensity before sunrise. VCWG predicted a maximum UHI of $+1.9$ K in Vancouver, in agreement with a measured maximum value of $+1.4$ K before sunrise (Runnalls, 1995; Lesnikowski, 2014; Ho et al., 2016). Case studies in Japan have reportedly obtained urban warming in large and developed cities such as Osaka, which is the interest in this study, and Tokyo in the afternoon (Leal Filho et al., 2017). This effect is also predicted by VCWG that showed the diurnally-averaged UHI of $+0.8$ K, which is consistent with other studies measuring a diurnally-averaged UHI of $+1.2$ K (Kusaka et al., 2012; Leal Filho et al., 2017). UHI in Copenhagen is reported to change between $+0.5$ and $+1.5$ K depending on the wind speed, which agrees reasonably well with the VCWG prediction of UHI varying from slightly negative values during the daytime to $+1.6$ K during the nighttime (Mahura et al., 2009).

3.2.7 Time Series Analysis

The VCWG was run for two weeks in August 2011 in Vancouver, Canada, to observe the day-to-day prediction of the temperature. Hourly time series of VCWG-predicted urban and rural temperatures with the corresponding EPW relative humidity, incoming direct and diffusive solar radiation, and mean horizontal wind speed in the rural area are shown in Fig. 16. The model can capture the cyclic pattern of temperature (and UHI) that is affected by the other forcing meteorological variables. For example, high UHI is mainly predicted during nighttime with preceding days dominated by high direct and diffuse incoming solar radiation and low wind speed. On the other hand, low UHI is mainly predicted during nighttime with preceding days dominated by attenuated incoming solar radiation and high wind speed.

4 Conclusions and Future Work

The Vertical City Weather Generator (VCWG) is an urban microclimate model designed to calculate vertical profiles of meteorological variables including potential temperature, wind speed, specific humidity, and turbulence kinetic energy in an urban area. The VCWG is composed of sub models for ingestion of urban parameters and meteorological variables in a rural area as

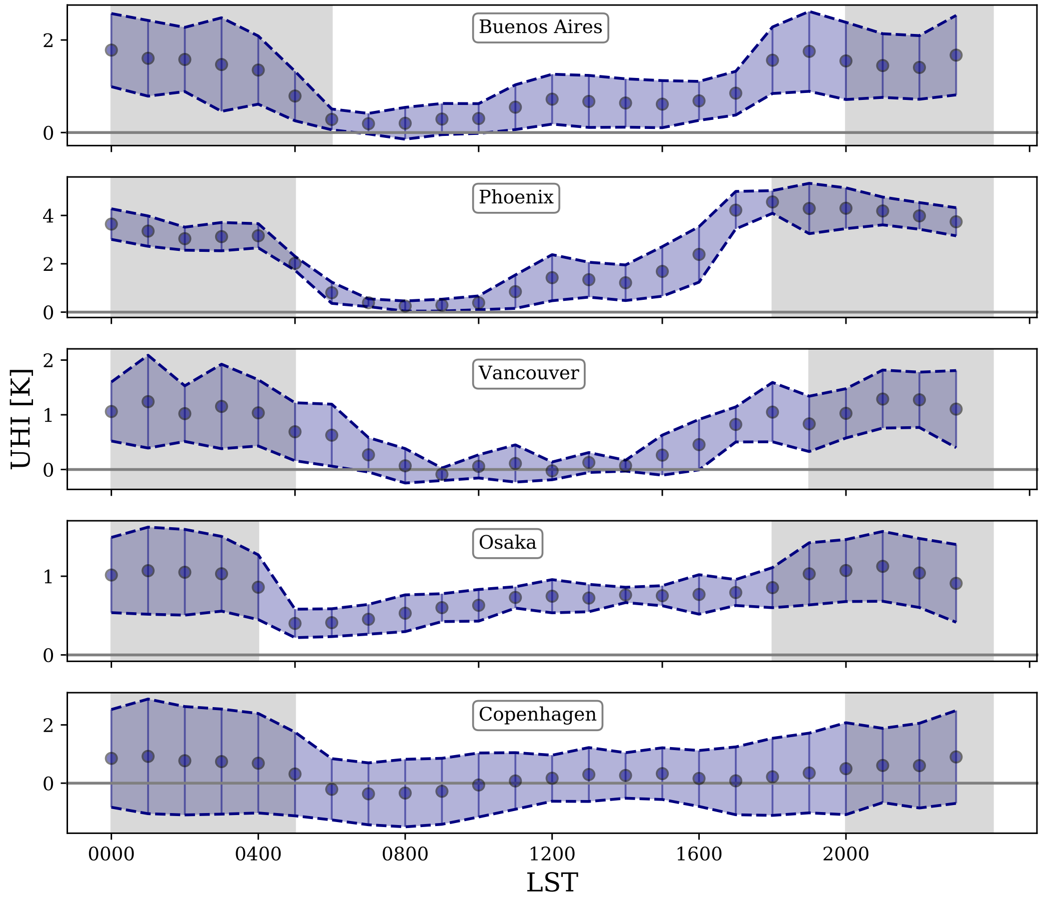

Figure 15. Diurnal variation of the UHIs in Buenos Aires, Phoenix, Vancouver, Osaka, and Copenhagen; diurnal variation of mean and standard deviation (error bar) are shown using data obtained over a two-week period; nighttime is shown with shaded regions; times in Local Standard Time (LST).

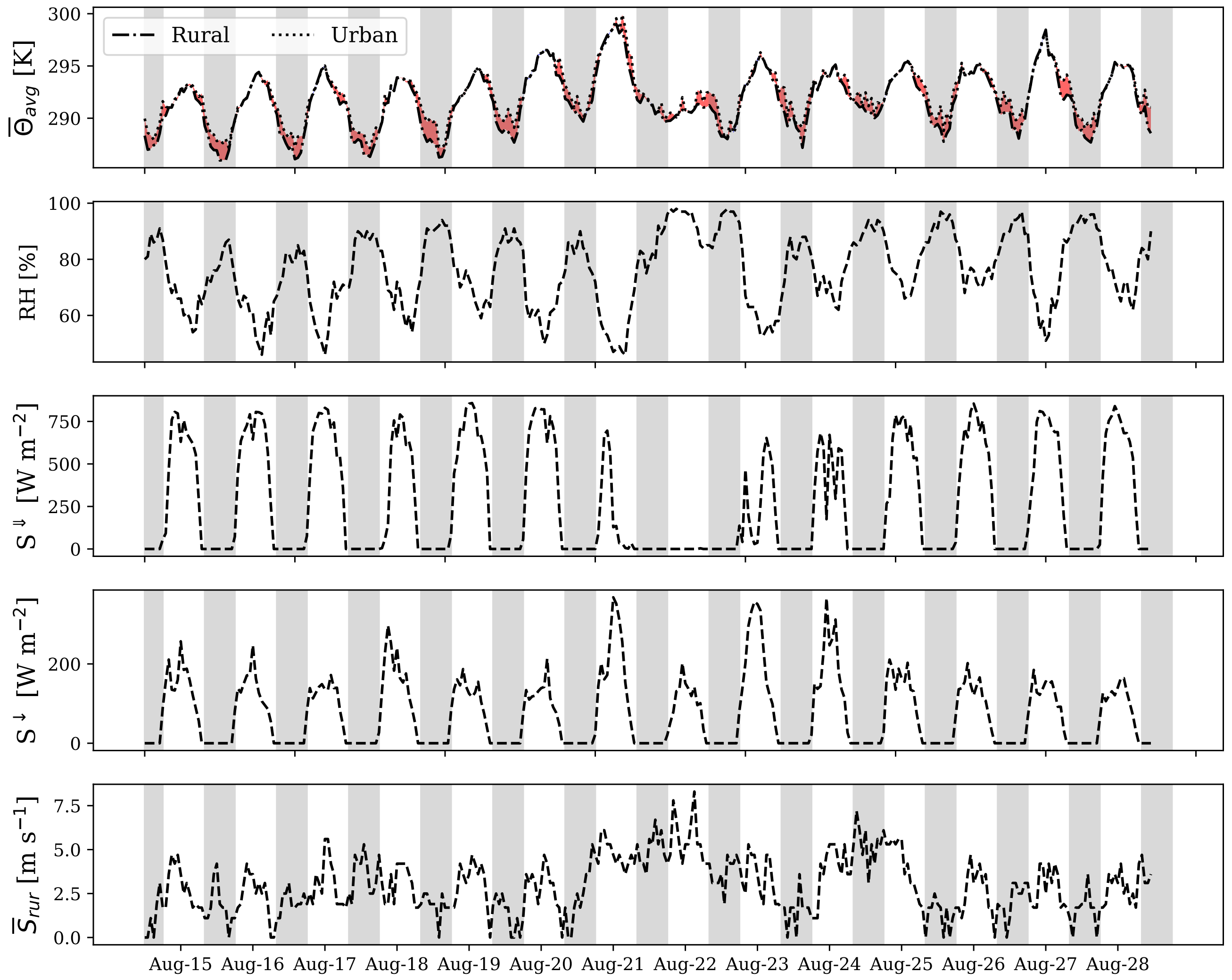

Figure 16. Hourly time series of rural and urban temperatures, rural relative humidity, rural incoming solar radiation, and rural mean horizontal wind speed in August 2011 in Vancouver, Canada; the shaded areas represent nighttime; positive UHI represented by shading the area between the temperature curves with red, while negative UHI represented by shading the area between the temperature curves with blue.

boundary conditions and prediction of the meteorological variables in a nearby urban area, the building energy performance variables, and the short and longwave radiation transfer processes. VCWG combines elements of several previous models developed by Loughner et al. (2012), Santiago and Martilli (2010), Bueno et al. (2014), Krayenhoff (2014), Krayenhoff et al. (2015), and Redon et al. (2017) to generate a model with the ability to predict vertical profiles of urban meteorological variables, forced by rural measurements, and with feedback interaction with both building energy and radiation models.

To evaluate VCWG, a microclimate field campaign was held from 15 July 2018 to 5 September 2018, in Guelph, Canada. The data was collected at the University of Guelph main campus representing an urban site and in the Guelph Turfgrass Institute, which is an open space to be considered as a nearby rural site. In the urban site, temperature, wind velocity components, relative humidity, and solar radiation were measured. In the rural site, the temperature and relative humidity at 2 m as well as wind speed and direction at 10 m were provided from a weather station by the World Meteorological Organization (WMO) dataset. The results obtained from VCWG agreed reasonably well with the measurements and predicted a $+1.2$ and $1.53\ \mathrm{K}$ mean and standard deviation, respectively, for Urban Heat Island (UHI) with reasonable agreement to observations reporting mean and standard deviation for UHI of $+1.8$ and $1.23\ \mathrm{K}$, respectively. The error analysis showed overall BIAS of $-1.43\ \mathrm{K}$, $1.06\ \mathrm{ms^{-1}}$, and $0.005\ \mathrm{kgkg^{-1}}$ for potential temperature, wind speed, and specific humidity, respectively. The analysis also showed overall RMSE of $1.56\ \mathrm{K}$, $1.32\ \mathrm{ms^{-1}}$, and $0.006\ \mathrm{kgkg^{-1}}$ for the same variables respectively.

The performance of the VCWG was further assessed by conducting seven types of explorations for both nighttime and daytime urban microclimate. First, we investigated how the urban geometry, which is characterized by plan area density λ_p and frontal area density λ_f, could affect the urban microclimate. Any increase in λ_p was associated with higher air temperatures and reduced wind speeds within the urban canyon. On the other hand, a configuration with higher λ_f increased shading effects and consequently reduced daytime temperatures, but it increased nighttime temperatures due to more heat released from urban surfaces that was trapped in the canyon. The cooling effect of the urban vegetation was also evaluated by changing the Leaf Area Density (LAD) profiles within the canyon. Increasing the average LAD showed heat removal from the canyon alongside with lower wind speeds due to the drag induced by trees. The VCWG was also run for different building types (a school and a small office), cooling system Coefficient of Performance (COP), and heating thermal efficiency. The results showed that a school generates more waste heat fluxes associated with gas consumption and water heating, which causes higher impact on the urban climate. The analysis of different cooling system also revealed that less-efficient system (lower COP and heating efficiency) resulted in more waste heat emission. The radiation model was assessed by running the VCWG for different canyon axis angles and canyon aspect ratio. The direct and diffusive solar radiation fluxes at the urban surfaces, and net longwave and shortwave solar radiation fluxes were compared. Net shortwave radiation flux was pronounced in less hours for the higher aspect ratio canyon, due to more shading effects on times before and after local noon. When the street canyon axis angle was perpendicular to the north axis, the net shortwave radiation fluxes were widened over a larger range of diurnal hours. Another exploration made for all months of the year justified the ability of the VCWG to predict the urban microclimate in different seasons. The result showed the expected diurnal variation of temperature profile in the urban site. The ability of the model to predict UHI in different cities with different climate zones was assessed. The case studies were Buenos Aires, Phoenix, Vancouver, Osaka, and Copenhagen. Finally, VCWG was able to produce realistic urban temperatures when it was run continuously for two weeks in Vancouver. All exploration results obtained from the VCWG were reasonably consistent with the previous studies in the literature.

In this study, it was shown that the urban microclimate model VCWG can successfully extend the spatial dimension of the preexisting bulk flow (single-layer) urban microclimate models to one-dimension in the vertical direction, while it also considers the relationship of the urban microclimate model to the rural meteorological measurements and the building energy conditions. The effect of the key urban elements such as building configuration, building energy systems, and vegetation were considered, but there is still opportunity to improve VCWG further. The urban site is simplified as blocks of buildings with symmetric and regular dimensions, which can be more realistically represented if more considerations were to be taken into account about nonuniform distribution of building dimensions. Future studies can also focus on improvement of flow-field parameterization or including additional source/sink terms in the transport equations to model horizontal motions, eddies, and flow fluctuations in the urban area, which is realistically very three-dimensional and heterogeneous. VCWG development can account for the spatial variation of urban microclimate in a computationally efficient manner independent of an auxiliary mesoscale model. This advantage is really important for urban planners, architects, and consulting engineers, to run VCWG operationally fast for many projects.

Code and data availability. The VCWG v1.1.0 is developed at the Atmospheric Innovations Research (AIR) Laboratory at the University of Guelph: http://www.aaa-scientists.com. The source code and the supporting environmental field monitoring data are available under GPL 3.0 licence: https://opensource.org/licenses/GPL-3.0 (last access: May 2019) and can be downloaded from https://www.zenodo.org/ with DOI: 10.5281/zenodo.3698344.

Appendix A

A1 Heat flux in the rural area

The net sensible heat fluxes at the surface level in the rural area can be decomposed into heat flux caused by vegetation, radiation flux absorbed by the surface, and the heat convection flux between the outer layer of soil and the atmosphere (see Eq. 6). The sensible heat flux from vegetation can be calculated as

$$Q_{Hveg,rur} = F_{veg}(1-F_{lat,grass})(1-\alpha_V)Q^{rec}_{rad,rur} \tag{A1}$$

where $\mathrm{F_{veg}}$ is the fraction of the rural area covered by vegetation, $\mathrm{F_{lat,grass}}$ is fraction of absorbed heat that is converted to an emitted latent heat flux, α_V is the albedo of the vegetation, and $\mathrm{Q^{rec}_{rad,rur}}$ is the solar radiation flux (direct plus diffuse components) received at the rural surface given in the weather file. The net solar radiation flux absorbed at the surface can be calculated from

$$Q_{rad,rur} = ((1-F_{veg})(1-\alpha_{rur}) + F_{veg}(1-\alpha_V))Q^{rec}_{rad,rur}, \tag{A2}$$

where α_rur is overall albedo of the rural area. The albedos of the rural area are input parameters in VCWG.

A2 Source/Sink Term in the 1-D Model

The pressure and skin drags exerted on the flow in Eq.s 8 and 9 are formulated as follows (Santiago and Martilli, 2010; Krayenhoff, 2014; Krayenhoff et al., 2015; Simón-Moral et al., 2017; Nazarian et al., 2019; Krayenhoff et al., 2020)

$$D_x = \underbrace{\frac{1}{\rho}\frac{\partial \tilde{P}}{\partial x}}_{I} + \underbrace{\nu(\nabla^2 \tilde{U})}_{II}, \tag{A3}$$

$$D_y = \underbrace{\frac{1}{\rho}\frac{\partial \tilde{P}}{\partial y}}_{I} + \underbrace{\nu(\nabla^2 \tilde{V})}_{II}, \tag{A4}$$

where term I represents dispersive pressure variation (form drag) induced by vegetation and building and term II represents the dispersive viscous dissipation (skin drag) induced by horizontal surfaces. The former can be parameterized as below

$$\frac{1}{\rho}\frac{\partial \tilde{P}}{\partial x} = \left(B_D C_{DBv} + LAD\Omega C_{DV}\right)\overline{U}_{expl}\overline{U}, \tag{A5}$$

$$\frac{1}{\rho}\frac{\partial \tilde{P}}{\partial y} = \left(B_D C_{DBv} + LAD\Omega C_{DV}\right)\overline{V}_{expl}\overline{V}, \tag{A6}$$

where $\mathrm{B_D}$ is sectional building area density, $\mathrm{C_{DBv}}$ is sectional drag coefficient in the presence of trees, LAD is leaf area density in the canyon, Ω is clumping factor, $\mathrm{C_{DV}}$ is the drag coefficient for tree foliage, and $\overline{\mathrm{U}}_{\mathrm{expl}}$ and $\overline{\mathrm{V}}_{\mathrm{expl}}$ are wind velocity components in x and y directions from a previous numerical solution, respectively, which are assumed explicitly as constants to linearize the system of equations to be solved. The skin drag can be parameterized as follow

$$\nu(\nabla^2 \tilde{U}) = c_d f_m \overline{U}_{expl}\overline{U}, \tag{A7}$$

$$\nu(\nabla^2 \tilde{V}) = c_d f_m \overline{V}_{expl}\overline{V}, \tag{A8}$$

where $\mathrm{c_d}$ is skin drag coefficient and $\mathrm{f_m}$ is a function of stability from Louis (1979).

The terms related to wake production $\mathrm{S_{wake}}$ and dissipation rate ε in Eq. 11 can be parameterized as

$$S_{wake} = \left(B_D C_{DBv} + LAD\Omega C_{DV}\right)\overline{U}^3_{expl}, \tag{A9}$$

$$\varepsilon = C_\varepsilon \frac{k^{\frac{3}{2}}}{\ell_{\varepsilon,dissip}}, \tag{A10}$$

where Ω is clumping factor, C_ε is a model constant and $\ell_{\varepsilon,\mathrm{dissip}}$ is a dissipation length scale obtained by sensitivity study using CFD (Nazarian et al., 2019).

The heat source/sink terms, terms in Eq. 12, caused by roof ($\mathrm{S_{\Theta R}}$) and ground ($\mathrm{S_{\Theta G}}$) are calculated based on the study by Louis (1979) and the heat flux from the wall ($\mathrm{S_{\Theta W}}$) is formulated in Martilli et al. (2002). The two other heat terms can be parameterized as below

$$S_{\Theta A} = \frac{4\rho_{abs}k_{air}}{\rho C_p v_L}\left[(1-\lambda_p)L_A\right], \tag{A11}$$

$$S_{\Theta V} = \frac{2g_{Ha}c_{PM}}{\rho C_p v_L}\left[LAD(1-\lambda_p)(\overline{\Theta}_V - \overline{\Theta})\right], \tag{A12}$$

where $\mathrm{L_A}$ is the absorbed flux density of longwave radiation in the canyon, ρ_{abs} is the density of absorbing molecules, $\mathrm{k_{air}}$ is their mass extinction cross section, $\mathrm{v_L}=(1-\lambda_{\mathrm{p}})$ is the fraction of total volume that is outdoor air, $\mathrm{g_{Ha}}$ is conductance for heat, $\mathrm{c_{PM}}$ is the molar heat capacity for the air, and $\overline{\Theta}_{\mathrm{V}}$ is the temperature of tree foliage.

In the specific humidity equation, the source/sink term can be calculated using the following equation

$$S_{QV} = \frac{\Lambda_M g_v \Omega}{\rho \Lambda v_L}\left[LAD(1-\lambda_p)(s[\overline{\Theta}_V - \overline{\Theta}]) + \frac{D}{P}\right] \tag{A13}$$

where Λ_{M} is molar latent heat of vaporization, $\mathrm{g_v}$ is the average surface and boundary-layer conductance for humidity for the whole leaf, D is the vapour deficit of the atmosphere, and P is atmospheric pressure.

A3 Building Heat Exchanges

The heat fluxes in Eq. 17 can be parameterized as bellow

$$Q_{surf} = \Sigma h_i A_i (T_{si} - T_{in}) \tag{A14}$$

$$Q_{inf} = \dot{m}_{inf} C_p (T_{out} - T_{in}) \tag{A15}$$

$$Q_{vent} = \dot{m}_{vent} C_p (T_{supp} - T_{in}) \tag{A16}$$

where $\mathrm{h_i}$ and $\mathrm{A_i}$ are convective heat transfer coefficient (or u-value) and surface area of indoor elements such as ceiling, walls, floor, building mass, and windows. $\mathrm{T_{si}}$ is the temperature of inner layer of elements, $\mathrm{T_{in}}$ is indoor temperature, $\mathrm{T_{out}}$ is the outdoor temperature averaged over building height, $\mathrm{T_{supp}}$ is supply temperature, $\dot{\mathrm{m}}_{\mathrm{inf}}$ is mass flow rate of infiltration (exfiltration), and $\dot{\mathrm{m}}_{\mathrm{vent}}$ is mass flow rate of ventilated air in the HVAC system.

A4 Longwave and Shortwave Radiation

For shortwave radiation fluxes, multiple reflections are considered. The total absorbed shortwave radiation flux by each urban element can be calculated by adding the first absorption of shortwave radiation flux before any reflection to the radiation flux received as a result of multiple reflections with the other elements. The following equations have been developed by Redon et al. (2017)

$$S_S = \Psi_{SG}\tau_{SG}(1-\delta_s)G_\infty + \Psi_{SV}\tau_{SV}\delta_s V_\infty + \Psi_{SW}\tau_{SW}W_\infty + \Psi_{ST}\delta_t T_\infty \tag{A17}$$

$$S_G = S_G^0 + (1-\alpha_G)\left[\Psi_{GW}\tau_{GW}W_\infty + c_{GT}\Psi_{GT}\delta_t T_\infty\right] \tag{A18}$$

$$S_V = S_V^0 + (1-\alpha_V)\left[\Psi_{VW}\tau_{VW}W_\infty + c_{VT}\Psi_{VT}\delta_t T_\infty\right] \tag{A19}$$

$$S_W = S_W^0 + (1-\alpha_W)\left[\Psi_{WG}\tau_{WG}(1-\delta_s)G_\infty + \Psi_{WV}\tau_{WV}\delta_s V_\infty + \Psi_{WW}\tau_{WW}\frac{W_\infty}{2} + c_{WT}\Psi_{WT}\delta_t T_\infty\right] \tag{A20}$$

$$S_T = \frac{1}{\delta_t}\left[(S^{\Downarrow} + S^{\downarrow}) - (S_S + (1-\delta_s)S_G + \delta_s S_V + \frac{2H_{avg}}{w}S_W)\right] \tag{A21}$$

where the subscripts ‘S’, ‘G’, ‘V’, ‘W’, and ‘T’ represent sky, ground, ground vegetation cover, wall, and tree, respectively. The superscript ‘0’ signifies the before-reflection absorption of shortwave radiation (described in detail in Redon et al. (2017)).

The view factor between two urban elements is shown by Ψ_{ij} with the suitable subscripts (e.g., i=G and j=W). For example Ψ_{GW} represents the view factor between ground and wall. Note that ground and ground vegetation cover have the same view factors with other surfaces, e.g. $\Psi_{\mathrm{GW}}=\Psi_{\mathrm{VW}}$. The total shortwave radiation reflected by ground, ground vegetation cover, wall, and trees are shown by G_{∞}, V_{∞}, W_{∞}, and T_{∞}, respectively (described in detail in Redon et al. (2017)). $\mathrm{S}^{\Downarrow}$ is direct incoming solar radiation, $\mathrm{S}^{\downarrow}$ is diffuse incoming solar radiation ($\mathrm{S}^{\Downarrow}$ and $\mathrm{S}^{\downarrow}$ are both obtained from the input weather file), c_{GT} and c_{VT} are model constants, τ_{ij} is radiative transmissivity between two elements (e.g. i=G and j=W), w is street width, $\mathrm{H}_{\mathrm{avg}}$ is average building height, δ_{t} is cover fraction of tree canopy, and δ_{s} is surface fraction covered by vegetation. The shading effect of trees are considered in the formulation of transmissivity (Lee and Park, 2008). Note that ground and ground vegetation cover have the same transmissivity with other surfaces, e.g. $\tau_{\mathrm{GW}}=\tau_{\mathrm{VW}}$.

For longwave radiation fluxes, multiple reflections are considered. The net longwave radiation fluxes received by the urban surfaces can be computed as (Loughner et al., 2012)

$$\begin{aligned}
L_W = \varepsilon_W \Big\{ & \tau_{WS}\Psi_{WS}L_S + \tau_{WG}((1-\delta_s)\varepsilon_G\Psi_{WG}\sigma T_G^4 + \delta_s\varepsilon_V\Psi_{WV}\sigma T_V^4) + \tau_{WW}\varepsilon_W\Psi_{WW}\sigma T_W^4 + L_{T\uparrow}^W \\
& - \sigma T_W^4 + \tau_{WG}\big[(1-\delta_s)(1-\varepsilon_G)\Psi_{WG}L_{T\uparrow}^G\big] + \tau_{WW}(1-\varepsilon_W)\Psi_{WW}L_{T\uparrow}^W \\
& + \tau_{WG}\tau_{WS}\big[(1-\delta_s)(1-\varepsilon_G)\Psi_{WG}\Psi_{GS}L_S + \delta_s(1-\varepsilon_V)\Psi_{WV}\Psi_{VS}L_S\big] \\
& + \tau_{WG}\tau_{WG}\big[(1-\delta_s)(1-\varepsilon_G)\Psi_{WG}\Psi_{WG}\varepsilon_W\sigma T_W^4 + \delta_s(1-\varepsilon_V)\Psi_{WG}\Psi_{WG}\varepsilon_W\sigma T_W^4\big] \\
& + \tau_{WW}\tau_{WG}\big[(1-\delta_s)(1-\varepsilon_W)\Psi_{WW}\Psi_{WG}\varepsilon_G\sigma T_G^4 + \delta_s(1-\varepsilon_W)\Psi_{WW}\Psi_{WG}\varepsilon_V\sigma T_V^4\big] \\
& + \tau_{WW}\tau_{WS}(1-\varepsilon_W)\Psi_{WW}\Psi_{WS}L_S + \tau_{WW}\tau_{WW}(1-\varepsilon_W)\Psi_{WW}\Psi_{WW}\varepsilon_W\sigma T_W^4 \Big\}
\end{aligned} \tag{A22}$$

$$\begin{aligned}
L_G = (1-\delta_s)\varepsilon_G \Big\{ & \tau_{GS}L_S\Psi_{GS} + \tau_{WG}\varepsilon_W\Psi_{WG}\sigma T_W^4 + L_{T\uparrow}^G - \sigma T_G^4 + \tau_{WG}(1-\varepsilon_W)\Psi_{GW}L_{T\uparrow}^W \\
& + \tau_{WG}\tau_{WS}(1-\varepsilon_W)\Psi_{GW}\Psi_{WS}L_S + \tau_{WG}\tau_{WW}\Psi_{GW}\Psi_{WW}\varepsilon_W\sigma T_W^4 \\
& + \tau_{WG}\tau_{WG}\big[(1-\delta_s)(1-\varepsilon_W)\Psi_{GW}\Psi_{WG}\varepsilon_G\sigma T_G^4 + \delta_s(1-\varepsilon_W)\Psi_{GW}\Psi_{WG}\varepsilon_V T_V^4\big] \Big\}
\end{aligned} \tag{A23}$$

$$\begin{aligned}
L_V = \delta_s\varepsilon_V \Big\{ & \tau_{GS}L_S\Psi_{GS} + \tau_{WG}\varepsilon_W\Psi_{WG}\sigma T_W^4 + L_{T\uparrow}^G - \sigma T_V^4 + \tau_{WG}(1-\varepsilon_W)\Psi_{GW}L_{T\uparrow}^W \\
& + \tau_{WG}\tau_{WS}(1-\varepsilon_W)\Psi_{GW}\Psi_{WS}L_S + \tau_{WG}\tau_{WW}\Psi_{GW}\Psi_{WW}\varepsilon_W\sigma T_W^4 \\
& + \tau_{WG}\tau_{WG}\big[(1-\delta_s)(1-\varepsilon_W)\Psi_{GW}\Psi_{WG}\varepsilon_G\sigma T_G^4 + \delta_s(1-\varepsilon_W)\Psi_{GW}\Psi_{WG}\varepsilon_V T_V^4\big] \Big\}
\end{aligned} \tag{A24}$$

$$L_T = L_S^T + L_T^T + L_G^T + L_V^T + L_W^T - L_{T\uparrow}, \tag{A25}$$

where the subscripts 'S', 'G', 'V', 'W', and 'T' represent sky, ground, ground vegetation cover, wall, and tree, respectively. L_{S} is radiative longwave flux emitted from the atmosphere/sky, T_{i} is surface temperature where i can be G, V, and W. $\mathrm{L}_{\mathrm{i}\uparrow}^{\mathrm{j}}$ is the longwave radiation emitted from surface i that reaches surface j. $\mathrm{L}_{\mathrm{S}}^{\mathrm{T}}$ represents the downwelling longwave radiation from the atmosphere above the street canyon that is absorbed by the tree canopy and $\mathrm{L}_{\mathrm{T}}^{\mathrm{T}}$, $\mathrm{L}_{\mathrm{G}}^{\mathrm{T}}$, $\mathrm{L}_{\mathrm{V}}^{\mathrm{T}}$, and $\mathrm{L}_{\mathrm{W}}^{\mathrm{T}}$ represent the longwave radiation emitted from the tree canopy, ground, ground vegetation cover, and walls, respectively, that is absorbed by the tree canopy. These terms account for multiple reflections from the walls, ground, and ground vegetation cover in the urban street canyon. $L_{T\uparrow}$ is total longwave radiation emitted from the tree canopy. A complete formulation of the terms in L_T is provided in detail in Loughner et al. (2012).

Author contributions. MM wrote the paper with significant conceptual input from ESK and AAA and critical feedback from all co-authors. BD, AN, MKN, and MRN operated the instruments in the field and partially analyzed resulting data. BB and LKN developed the base Urban Weather Generator (UWG) program in MATLAB. CM and SV translated UWG from MATLAB to Python. NN and ESK provided their code for the one-dimensional vertical diffusion model for the urban climate that was integrated into VCWG. MM and AAA developed the Vertical City Weather Generator (VCWG) program in Python by integrating various modeling components developed by BB, LKN, CM, SV, ESK, and NN.

Competing interests. The authors declare that they have no conflict of interest.

Acknowledgements. The authors are indebted to Steve Nyman, Chris Duiker, Peter Purvis, Manuela Racki, Jeffrey Defoe, Joanne Ryks, Ryan Smith, James Bracken, and Samantha French at the University of Guelph, who helped with the campaign logistics. Special credit is directed toward Amanda Sawlor, Esra Mohamed, Di Cheng, Randy Regan, Margaret Love, Angela Vuk, and Carolyn Dowling-Osborn at the University of Guelph for administrative support. The computational platforms were set up with the assistance of Jeff Madge, Joel Best, and Matthew Kent at the University of Guelph. The authors thank Alberto Martilli at Centre for Energy, Environment and Technology (CIEMAT) in Madrid, Spain, who developed and shared an earlier version of the one-dimensional vertical diffusion model for the urban climate. The authors also thank William D. Lubitz for providing three ultrasonic anemometers for the field campaign.

This work was supported by the University of Guelph through the International Graduate Tuition Scholarship (IGTS) for the lead author; Philanthropic contributions from Professor Edward McBeans's Foundation toward acquisition of experimental equipment; Discovery Grant program (401231) from the Natural Sciences and Engineering Research Council (NSERC) of Canada; Government of Ontario through the Ontario Centres of Excellence (OCE) under the Alberta-Ontario Innovation Program (AOIP) (053450); and Emission Reduction Alberta (ERA) (053498). OCE is a member of the Ontario Network of Entrepreneurs (ONE).

References

Adnot, J., Riviere, P., Marchio, D., Becirspahic, S., Lopes, C., Blanco, I., Perez-Lombard, L., Ortiz, J., Papakonstantnou, N., Doukas, P., et al.: Energy efficiency and certification of central air conditioners (EECCAC), Study for the DG Transportation-Energy (DGTREN) of the Commission of the EU, Paris, 2003.

Akbari, H., Pomerantz, M., and Taha, H.: Cool surfaces and shade trees to reduce energy use and improve air quality in urban areas, Sol. Energy, 70, 295–310, 2001.

Aliabadi, A. A., Krayenhoff, E. S., Nazarian, N., Chew, L. W., Armstrong, P. R., Afshari, A., and Norford, L. K.: Effects of roof-edge roughness on air temperature and pollutant concentration in urban canyons, Bound.-Lay. Meteorol., 164, 249–279, 2017.

Aliabadi, A. A., Veriotes, N., and Pedro, G.: A Very Large-Eddy Simulation (VLES) model for the investigation of the neutral atmospheric boundary layer, Journal of Wind Engineering and Industrial Aerodynamics, 183, 152–171, 2018.

Aliabadi, A. A., Moradi, M., Clement, D., Lubitz, W. D., and Gharabaghi, B.: Flow and temperature dynamics in an urban canyon under a comprehensive set of wind directions, wind speeds, and thermal stability conditions, Environ. Fluid Mech., 19, 81–109, 2019.

Armson, D., Stringer, P., and Ennos, A.: The effect of tree shade and grass on surface and globe temperatures in an urban area, Urban For. Urban Gree., 11, 245–255, 2012.

Balogun, A. A., Tomlin, A. S., Wood, C. R., Barlow, J. F., Belcher, S. E., Smalley, R. J., Lingard, J. J. N., Arnold, S. J., Dobre, A., Robins, A. G., Martin, D., and Shallcross, D. E.: In-street wind direction variability in the vicinity of a busy intersection in central London, Bound.-Lay. Meteorol., 136, 489–513, 2010.

Bejarán, R. and Camilloni, I.: Objective method for classifying air masses: an application to the analysis of Buenos Aires'(Argentina) urban heat island intensity, Theor. Appl. Climatol., 74, 93–103, 2003.

Blocken, B.: Computational Fluid Dynamics for urban physics: Importance, scales, possibilities, limitations and ten tips and tricks towards accurate and reliable simulations, Build. Environ., 91, 219–245, 2015.

Bornstein, R. D.: The Two-Dimensional URBMET Urban Boundary Layer Model, J. Appl. Meteorol., 14, 1459–1477, 1975.

Britter, R. E. and Hanna: Flow and Dispersion in Urban Areas, Annu. Rev. Fluid Mech, 35, 469–496, 2003.

Broadbent, A. M., Coutts, A. M., Nice, K. A., Demuzere, M., Krayenhoff, E. S., Tapper, N. J., and Wouters, H.: The Air-temperature Response to Green/blue-infrastructure Evaluation Tool (TARGET v1. 0): an efficient and user-friendly model of city cooling, Geosci. Model Dev., 12, 785–803, 2019.

Bueno, B., Norford, L. K., Pigeon, G., and Britter, R.: Combining a detailed building energy model with a physically-based urban canopy model, Bound.-Lay. Meteorol., 140, 471–489, 2011.

Bueno, B., Norford, L. K., Hidalgo, J., and Pigeon, G.: The urban weather generator, J. Build. Perf. Simulat., 6, 269–281, 2012a.

Bueno, B., Pigeon, G., Norford, L. K., Zibouche, K., and Marchadier, C.: Development and evaluation of a building energy model integrated in the TEB scheme, Geosci. Model Dev., pp. 433–448, 2012b.

Bueno, B., Roth, M., Norford, L. K., and Li, R.: Computationally efficient prediction of canopy level urban air temperature at the neighbourhood scale, Urban Climate, 9, 35–53, 2014.

Businger, J. A., Wyngaard, J. C., Izumi, Y., and Bradley, E. F.: Flux-profile relationships in the atmospheric surface layer, J. Atmos. Sci., 28, 181–189, 1971.

Chen, F., Kusaka, H., Bornstein, R., Ching, J., Grimmond, C. S. B., Grossman-Clarke, S., Loridan, T., Manning, K. W., Martilli, A., Miao, S., Sailor, D., Salamanca, F. P., Taha, H., Tewari, M., Wang, X., Wyszogrodzki, A. A., and Zhang, C.: The integrated WRF/urban modelling system: development, evaluation, and applications to urban environmental problems, Int. J. Climatol., 31, 273–288, 2011.

Chin, H.-N. S., Leach, M. J., Sugiyama, G. A., Leone Jr, J. M., Walker, H., Nasstrom, J., and Brown, M. J.: Evaluation of an Urban Canopy Parameterization in a Mesoscale Model Using VTMX and URBAN 2000 Data, Mon. Weather Rev., 133, 2043–2068, 2005.

Ciccioli, P., Fabozzi, C., Brancaleoni, E., Cecinato, A., Frattoni, M., Cieslik, S., Kotzias, D., Seufert, G., Foster, P., and Steinbrecher, R.: Biogenic emission from the Mediterranean pseudosteppe ecosystem present in Castelporziano, Atmos. Environ., 31, 167–175, 1997.

Coceal, O. and Belcher, S.: A canopy model of mean winds through urban areas, Q. J. R. Meteorol. Soc., 130, 1349–1372, 2004.

Conry, P., Fernando, H., Leo, L., Sharma, A., Potosnak, M., and Hellmann, J.: Multi-scale simulations of climate-change influence on Chicago Heat Island, in: ASME 2014 4th Joint US-European Fluids Engineering Division Summer Meeting collocated with the ASME 2014 12th International Conference on Nanochannels, Microchannels, and Minichannels, American Society of Mechanical Engineers, 2014.

Coutts, A. M., Beringer, J., and Tapper, N. J.: Impact of Increasing Urban Density on Local Climate: Spatial and Temporal Variations in the Surface Energy Balance in Melbourne, Australia, J. Appl. Meteorol. Clim., 46, 477–493, 2007.

Crank, P. J., Sailor, D. J., Ban-Weiss, G., and Taleghani, M.: Evaluating the ENVI-met microscale model for suitability in analysis of targeted urban heat mitigation strategies, Urban climate, 26, 188–197, 2018.

Dupont, S., Otte, T. L., and Ching, J. K. S.: Simulation of Meteorological Fields Within and Above Urban and Rural Canopies with a Mesoscale Model, Bound.-Lay. Meteorol., 113, 111–158, 2004.

Dyer, A.: A review of flux-profile relationships, Bound.-Lay. Meteorol., 7, 363–372, 1974.

Emmanuel, R. and Steemers, K.: Connecting the realms of urban form, density and microclimate, Build. Res. Inf., 46, 804–808, 2018.

Erell, E. and Williamson, T.: Simulating air temperature in an urban street canyon in all weather conditions using measured data at a reference meteorological station, Int. J. Climatol., 26, 1671–1694, 2006.

Fast, J. D., Torcolini, J. C., and Redman, R.: Pseudovertical Temperature Profiles and the Urban Heat Island Measured by a Temperature Datalogger Network in Phoenix, Arizona, J. Appl. Meteorol., 44, 3–13, 2005.

Futcher, J. A.: 658-ICE TEA CITY, in: 25th Conference on Passve and Low Energy Architecture, 2008.

Giometto, M., Christen, A., Egli, P., Schmid, M., Tooke, R., Coops, N., and Parlange, M.: Effects of trees on mean wind, turbulence and momentum exchange within and above a real urban environment, Adv. Water Resour., 106, 154–168, 2017.

Giometto, M. G., Christen, A., Meneveau, C., Fang, J., Krafczyk, M., and Parlange, M. B.: Spatial Characteristics of Roughness Sublayer Mean Flow and Turbulence Over a Realistic Urban Surface, Bound.-Lay. Meteorol., 160, 425–452, 2016.

Gowardhan, A. A., Pardyjak, E. R., Senocak, I., and Brown, M. J.: A CFD-based wind solver for an urban fast response transport and dispersion model, Environ. Fluid Mech., 11, 439–464, 2011.

Grimmond, C. S. B. and Oke, T. R.: Aerodynamic Properties of Urban Areas Derived from Analysis of Surface Form, J. Appl. Meteorol., 38, 1262–1292, 1999.

Grimmond, C. S. B., Souch, C., and Hubble, M. D.: Influence of tree cover on summertime surface energy balance fluxes, San Gabriel Valley, Los Angeles, Clim. Res., 6, 45–57, 1996.

Gros, A., Bozonnet, E., and Inard, C.: Cool materials impact at district scale: Coupling building energy and microclimate models, Sustain. Cities Soc., 13, 254–266, 2014.

Hamdi, R. and Masson, V.: Inclusion of a Drag Approach in the Town Energy Balance (TEB) Scheme: Offline 1D Evaluation in a Street Canyon, J. Appl. Meteorol. Clim., 47, 2627–2644, 2008.

Hawkins, T. W., Brazel, A. J., Stefanov, W. L., Bigler, W., and Saffell, E. M.: The Role of Rural Variability in Urban Heat Island Determination for Phoenix, Arizona, J. Appl. Meteorol., 43, 476–486, 2004.

Ho, H. C., Knudby, A., Xu, Y., Hodul, M., and Aminipouri, M.: A comparison of urban heat islands mapped using skin temperature, air temperature, and apparent temperature (Humidex), for the greater Vancouver area, Sci. Total Environ., 544, 929–938, 2016.

Jamei, E., Rajagopalan, P., Seyedmahmoudian, M., and Jamei, Y.: Review on the impact of urban geometry and pedestrian level greening on outdoor thermal comfort, Renew. Sust. Energ. Rev., 54, 1002–1017, 2016.

Joffre, S., Kangas, M., Heikinheimo, M., and Kitaigorodskii, S.: Variability of the Stable and Unstable Atmospheric Boundary-Layer Height and its Scales Over a Boreal Forest, Bound.-Lay. Meteorol., 99, 429–450, 2001.

Kang, W. and Sung, H. J.: Large-scale structures of turbulent flows over an open cavity, J. Fluid Struct., 25, 1318–1333, 2009.

Kastner-Klein, P., Berkowicz, R., and Britter, R.: The influence of street architecture on flow and dispersion in street canyons, Meteorol. Atmos. Phys, 87, 121–131, 2004.

Kikegawa, Y., Genchi, Y., Yoshikado, H., and Kondo, H.: Development of a numerical simulation system toward comprehensive assessments of urban warming countermeasures including their impacts upon the urban buildings' energy-demands, Appl. Energ., 76, 449–466, 2003.

Kleerekoper, L., van Esch, M., and Salcedo, T. B.: How to make a city climate-proof, addressing the urban heat island effect, Resour. Conserv. Recy., 64, 30–38, 2012.

Kochanski, A., Pardyjak, E., Stoll, R., Gowardhan, A., Brown, M., and Steenburgh, W.: One-Way Coupling of the WRF-QUIC Urban Dispersion Modeling System, J. Appl. Meteorol. Clim., 54, 2119–2139, 2015.

Kondo, H., Genchi, Y., Kikegawa, Y., Ohashi, Y., Yoshikado, H., and Komiyama, H.: Development of a Multi-Layer Urban Canopy Model for the Analysis of Energy Consumption in a Big City: Structure of the Urban Canopy Model and its Basic Performance, Bound.-Lay. Meteorol., 116, 395–421, 2005.

Kono, T., Ashie, Y., and Tamura, T.: Mathematical Derivation of Spatially-Averaged Momentum Equations for an Urban Canopy Model Using Underlying Concepts of the Immersed Boundary Method, Bound.-Lay. Meteorol., 135, 185–207, 2010.

Krayenhoff, E., Christen, A., Martilli, A., and Oke, T.: A Multi-Layer Radiation Model for Urban Neighbourhoods with Trees, Bound.-Lay. Meteorol., 151, 139–178, 2014.

Krayenhoff, E. S.: A multi-layer urban canopy model for neighbourhoods with trees, Ph.D. thesis, University of British Columbia, 2014.

Krayenhoff, E. S. and Voogt, J. A.: A Microscale Three-Dimensional Urban Energy Balance Model for Studying Surface Temperatures, Bound.-Layer Meteorol., 123, 433–461, 2007.

Krayenhoff, E. S., Santiago, J.-L., Martilli, A., Christen, A., and Oke, T. R.: Parametrization of Drag and Turbulence for Urban Neighbourhoods with Trees, Bound.-Lay. Meteorol., 156, 157–189, 2015.

Krayenhoff, E. S., Jiang, T., Christen, A., Martilli, A., Oke, T. R., Bailey, B. N., Nazarian, N., Voogt, J. A., Giometto, M. G., Stastny, A., et al.: A multi-layer urban canopy meteorological model with trees (BEP-Tree): Street tree impacts on pedestrian-level climate, Urban Climate, 32, 100 590, 2020.

Kusaka, H., Kondo, H., Kikegawa, Y., and Kimura, F.: A Simple Single-Layer Urban Canopy Model for Atmospheric Models: Comparison with Multi-Layer and Slab Models, Bound.-Lay. Meteorol., 101, 329–358, 2001.

Kusaka, H., Hara, M., and Takane, Y.: Urban Climate Projection by the WRF Model at 3-km Horizontal Grid Increment: Dynamical Downscaling and Predicting Heat Stress in the 2070's August for Tokyo, Osaka, and Nagoya Metropolises, J. Meteorol. Soc. Jpn. Ser. II, 90, 47–63, 2012.

Leal Filho, W., Echevarria Icaza, L., Emanche, V., and Quasem Al-Amin, A.: An Evidence-Based Review of Impacts, Strategies and Tools to Mitigate Urban Heat Islands, Int. J. Env. Res. Pub. He., 14, 1600, 2017.

Lee, S.-H. and Park, S.-U.: A Vegetated Urban Canopy Model for Meteorological and Environmental Modelling, Bound.-Lay. Meteorol., 126, 73–102, 2008.

Lesnikowski, A.: Adaptation to urban heat island effect in Vancouver, BC: A case study in analyzing vulnerability and adaptation opportunities, Ph.D. thesis, University of British Columbia, 2014.

Loughner, C. P., Allen, D. J., Zhang, D.-L., Pickering, K. E., Dickerson, R. R., and Landry, L.: Roles of Urban Tree Canopy and Buildings in Urban Heat Island Effects: Parameterization and Preliminary Results, J. Appl. Meteorol. Clim., 51, 1775–1793, 2012.

Louis, J.-F.: A Parametric Model of Vertical Eddy Fluxes in the Atmosphere, Bound.-Lay. Meteorol., 17, 187–202, 1979.

Lundquist, K. A., Chow, F. K., and Lundquist, J. K.: An Immersed Boundary Method for the Weather Research and Forecasting Model, Mon. Weather Rev., 138, 796–817, 2010.

Mahura, A., Baklanov, A., Petersen, C., Nielsen, N. W., and Amstrup, B.: Verification and Case Studies for Urban Effects in HIRLAM Numerical Weather Forecasting, in: Meteorological and Air Quality Models for Urban Areas, pp. 143–150, Springer, 2009.

Maronga, B., Gryschka, M., Heinze, R., Hoffmann, F., Kanani-Sühring, F., Keck, M., Ketelsen, K., Letzel, M. O., Sühring, M., and Raasch, S.: The Parallelized Large-Eddy Simulation Model (PALM) version 4.0 for atmospheric and oceanic flows: model formulation, recent developments, and future perspectives, Geosci. Model Dev., 8, 2515–2551, 2015.

Martilli, A. and Santiago, J. L.: CFD simulation of airflow over a regular array of cubes. Part II: analysis of spatial average properties, Bound.-Lay. Meteorol., 122, 635–654, 2007.

Martilli, A., Clappier, A., and Rotach, M. W.: An Urban Surface Exchange Parameterisation for Mesoscale Models, Bound.-Lay. Meteorol., 104, 261–304, 2002.

Masson, V.: A Physically-Based Scheme for the Urban Energy Budget in Atmospheric Models, Bound.-Lay. Meteorol., 94, 357–397, 2000.

Masson, V., Grimmond, C. S. B., and Oke, T. R.: Evaluation of the Town Energy Balance (TEB) Scheme with Direct Measurements from Dry Districts in Two Cities, J. Appl. Meteorol., 41, 1011–1026, 2002.

Masson, V., Gomes, L., Pigeon, G., Liousse, C., Pont, V., Lagouarde, J. P., Voogt, J., Salmond, J., Oke, T. R., Hidalgo, J., Legain, D., Garrouste, O., Lac, C., Connan, O., Briottet, X., Lachérade, S., and Tulet, P.: The Canopy and Aerosol Particles Interactions in TOlouse Urban Layer (CAPITOUL) experiment, Meterol. Atmos. Phys., 102, 135–157, 2008.

Mauree, D., Blond, N., and Clappier, A.: Multi-scale modeling of the urban meteorology: Integration of a new canopy model in the WRF model, Urban Climate, 26, 60–75, 2018.

Mills, G.: An urban canopy-layer climate model, Theor. Appl. Climatol., 57, 229–244, 1997.

Moeng, C., Dudhia, J., Klemp, J., and Sullivan, P.: Examining Two-Way Grid Nesting for Large Eddy Simulation of the PBL Using the WRF Model, Mon. Weather Rev., 135, 2295–2311, 2007.

Monin, A. S. and Obukhov, A. M.: Basic regularity in turbulent mixing in the surface layer of the atmosphere, Tr. Akad. Nauk SSSR Geophiz. Inst., 1957.

Nazarian, N. and Kleissl, J.: Realistic solar heating in urban areas: air exchange and street-canyon ventilation, Build. Environ., 95, 75–93, 2016.

Nazarian, N., Martilli, A., and Kleissl, J.: Impacts of Realistic Urban Heating, Part I: Spatial Variability of Mean Flow, Turbulent Exchange and Pollutant Dispersion, Bound.-Lay. Meteorol., 166, 367–393, 2018.

Nazarian, N., Krayenhoff, E. S., and Martilli, A.: A One-Dimensional Model of Turbulent Flow Through 'Urban' Canopies: Updates Based on Large-Eddy Simulation, Geosci. Model Dev. Discussions, 2019, 1–24, 2019.

Oke, T. R., Mills, G., Christen, A., and Voogt, J. A.: Urban Climates, Cambridge University Press, 2017.

Palyvos, J.: A survey of wind convection coefficient correlations for building envelope energy systems' modeling, Appl. Therm Eng., 28, 801–808, 2008.

Perret, L. and Savory, E.: Large-Scale Structures Over a Single Street Canyon Immersed in an Urban-Type Boundary Layer, Bound.-Lay. Meteorol., 148, 111–131, 2013.

Pope, S. B.: Turbulent flows, Cambridge University Press, Cambridge, U.K., 2000.

Redon, E. C., Lemonsu, A., Masson, V., Morille, B., and Musy, M.: Implementation of street trees within the solar radiative exchange parameterization of TEB in SURFEX v8. 0, Geosci. Model Dev., 10, 385–411, 2017.

Resler, J., Krč, P., Belda, M., Juruš, P., Benešová, N., Lopata, J., Vlček, O., Damašková, D., Eben, K., Derbek, P., Maronga, B., and Kanani-Sühring, F.: PALM-USM v1. 0: A new urban surface model integrated into the PALM large-eddy simulation model, Geosci. Model Dev., 10, 3635–3659, 2017.

Roth, M.: Review of atmospheric turbulence over cities, Q. J. R. Meteorol. Soc., 126, 941–990, 2000.

Runnalls, K. E.: Temporal dynamics of Vancouver's urban heat island, Ph.D. thesis, University of British Columbia, 1995.

Ryu, Y.-H., Baik, J.-J., and Lee, S.-H.: A New Single-Layer Urban Canopy Model for Use in Mesoscale Atmospheric Models, J. Appl. Meteorol. Clim., 50, 1773–1794, 2011.

Salamanca, F., Krpo, A., Martilli, A., and Clappier, A.: A new building energy model coupled with an urban canopy parameterization for urban climate simulations—part I. formulation, verification, and sensitivity analysis of the model, Theor. Appl. Climatol., 99, 331–344, 2010.

Salamanca, F., Georgescu, M., Mahalov, A., Moustaoui, M., and Wang, M.: Anthropogenic heating of the urban environment due to air conditioning, J. Geophys. Res.-Atmos., 119, 5949–5965, 2014.

Salizzoni, P., Marro, M., Soulhac, L., Grosjean, N., and Perkins, R. J.: Turbulent Transfer Between Street Canyons and the Overlying Atmospheric Boundary Layer, Bound.-Lay. Meteorol., 141, 393–414, 2011.

Saneinejad, S., Moonen, P., Defraeye, T., Derome, D., and Carmeliet, J.: Coupled CFD, radiation and porous media transport model for evaluating evaporative cooling in an urban environment, J. Wind. Eng. Ind. Aerodyn., 104, 455–463, 2012.

Santiago, J. L. and Martilli, A.: A Dynamic Urban Canopy Parameterization for Mesoscale Models Based on Computational Fluid Dynamics Reynolds-Averaged Navier-Stokes Microscale Simulations, Bound.-Lay. Meteorol., 137, 417–439, 2010.

Santiago, J. L., Krayenhoff, E. S., and Martilli, A.: Flow simulations for simplified urban configurations with microscale distributions of surface thermal forcing, Urban Climate, 9, 115–133, 2014.

Simón-Moral, A., Santiago, J. L., and Martilli, A.: Effects of Unstable Thermal Stratification on Vertical Fluxes of Heat and Momentum in Urban Areas, Bound.-Lay. Meteorol., 163, 103–121, 2017.

Souch, C. and Souch, C.: The effect of trees on summertime below canopy urban climates: a case study Bloomington, Indiana, J. Arboriculture, 19, 303–312, 1993.

Soulhac, L., Salizzoni, P., Cierco, F.-X., and Perkins, R.: The model SIRANE for atmospheric urban pollutant dispersion; part I, presentation of the model, Atmos. Environ., 45, 7379–7395, 2011.

Stull, R. B.: An Introduction to Boundary Layer Meteorology, Kluwer Academic Publishers, Dordrecht, The Netherlands, 1988.

Talbot, C., Bou-Zeid, E., and Smith, J.: Nested mesoscale large-eddy simulations with WRF: performance in real test cases, J. Hydrometeorol., 13, 1421–1441, 2012.

Tseng, Y.-H., Meneveau, C., and Parlange, M. B.: Modeling flow around bluff bodies and predicting urban dispersion using large eddy simulation, Environ. Sci. Technol., 40, 2653–2662, 2006.

van der Kooi, C. J., Kevan, P. G., and Koski, M. H.: The thermal ecology of flowers, Ann. Bot-London, 124, 343–353, 2019.

Wang, H., Skamarock, W. C., and Feingold, G.: Evaluation of Scalar Advection Schemes in the Advanced Research WRF Model Using Large-Eddy Simulations of Aerosol-Cloud Interactions, Mon. Weather Rev., 137, 2547–2558, 2009.

Wong, M. S., Nichol, J. E., To, P. H., and Wang, J.: A simple method for designation of urban ventilation corridors and its application to urban heat island analysis, Build. Environ., 45, 1880–1889, 2010.

Yaghoobian, N. and Kleissl, J.: Effect of reflective pavements on building energy use, Urban Climate, 2, 25–42, 2012.

Yang, X. and Li, Y.: The impact of building density and building height heterogeneity on average urban albedo and street surface temperature, Build. Environ., 90, 146–156, 2015.

Yuan, C., Norford, L. K., and Ng, E.: A semi-empirical model for the effect of trees on the urban wind environment, Landscape Urban Plan., 168, 84–93, 2017.

Zajic, D., Fernando, H. J. S., Calhoun, R., Princevac, M., Brown, M. J., and Pardyjak, E. R.: Flow and Turbulence in an Urban Canyon, J. Appl. Meteorol. Clim., 50, 203–223, 2011.